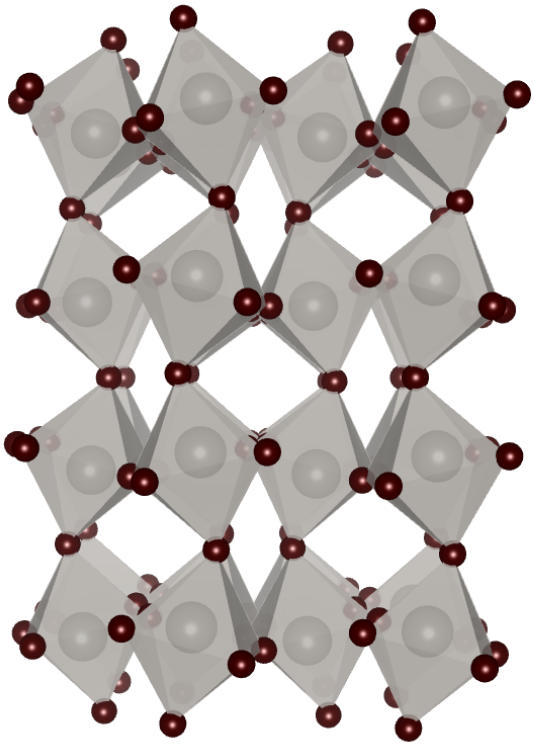

Structural and thermodynamical properties of tungsten oxides from first-principles calculations

Master's thesis in Applied Physics

CHRISTOPHER LINDERÄLV

Department of Physics
Chalmers University of Technology
Gothenburg, Sweden 2016

Structural and thermodynamical properties of tungsten oxides from first-principles calculations

CHRISTOPHER LINDERÄLV

Department of Physics
Division of Materials and Surface Theory
Chalmers University of Technology
Gothenburg, Sweden 2016

Structural and thermodynamical properties of tungsten oxides from first-principles calculations
CHRISTOPHER LINDERÄLV

Supervisor: Paul Erhart, Department of Physics
Examiner: Paul Erhart, Department of Physics

Department of Physics
Division of Materials and Surface Theory
Chalmers University of Technology
SE-412 96 Gothenburg
Telephone +46 31 772 1000

Cover: Crystal structure for ground state WO_3.

Typeset in LaTeX
Printed by Chalmers reproservice
Gothenburg, Sweden 2016

Structural and thermodynamical properties of tungsten oxides from first-principles calculations

CHRISTOPHER LINDERÄLV
Department of Physics
Chalmers University of Technology

Abstract

Tungsten as a material has obtained attention because of its prominent role in fusion reactor design, where it is employed in the divertor region of the first wall. In case of an accident, the tungsten tiles may be exposed to atmospheric conditions and high temperatures which would oxidize the material.

Over the years there has been a lot of studies on tungsten oxides, specially WO_3, but not from the perspective of tungsten oxidation. The mechanism of oxidation is unclear and a sound understanding of which oxides are formed is still lacking.

In this work, first principles calculations have been employed to study the relative phase stabilities from a mechanical and thermodynamical perspective. Oxidation has been studied using a point defect approach to the formation and migration energies of oxygen in tungsten and tungsten oxides. Using the same approach, the role of Y substitutional defects has been studied.

Tungsten trioxide is thermodynamically stable with respect to tungsten dioxide but is not as dynamically stable as tungsten dioxide. Oxygen interstitials have a low formation and migration energy in tungsten and several interstitials tend to pair up to form stable clusters, while interstitials in the oxide phases have higher formation energies. In the oxide phases the oxygen vacancy is associated with high formation energies. The difference in phonon frequencies between a pure system and the Y substitutional system is found to be small.

The main oxide, tungsten trioxide, is predicted to be dynamically unstable with imaginary phonon frequencies. Therefore, the active components should be chosen such that the mechanical properties of the formed oxide are enhanced. In this study the Y substitutional is found to have no stabilizing effect on tungsten trioxide, however, the full phonon dispersion for the defect system has not been obtained yet.

Keywords: tungsten, DFT, phonons, point defects, oxidation, fusion

Acknowledgements

I would like to thank my supervisor Paul Erhart for guiding me through this project and for always taking time to answer questions and helping me with the scientific writing. I also want to thank Anders Lindman for useful inputs and theory related discussions. I would also like to thank all members of the Division of Materials and Surface theory for all the help and for creating a friendly and inspiring work environment.

Christopher Linderälv, Gothenburg, June 2016

Contents

1 Background

This section begins with a description of the applications of tungsten oxides. After that, the oxides that this work focuses on are presented. This section then ends with a brief explanation of concepts that are central in this work such as phonons and crystal defects.

1.1 Introduction

Constructing modern fusion reactors, engineers are faced with the problem of constructing a reactor holding a confined plasma of about one hundred million degrees celsius and extracting energy from it. In the Tokamak design, which is one of the most common fusion reactor designs, the plasma is confined in an electromagnetic field in a torus-shaped vacuum vessel. During operation there will inevitably be some contact with materials because the fusion ash and heat has to be extracted from the reactor. Heat is mostly extracted as radiation but high energy particles can also be used to generate electricity.

The estimated operating temperature at the wall in the Tokamak design, which is the design chosen for the International Thermonuclear Experimental Reactor (ITER), can reach values of around 2400 K [1]. The high operating temperature requires a material that can lead away heat sufficiently fast to avoid melting. The fusion ash and heat in the form of high energy plasma particles is extracted from the bottom of the reactor via the so called divertor. The torus-shaped vacuum vessel and the cross-section is shown in Figure 1.1.

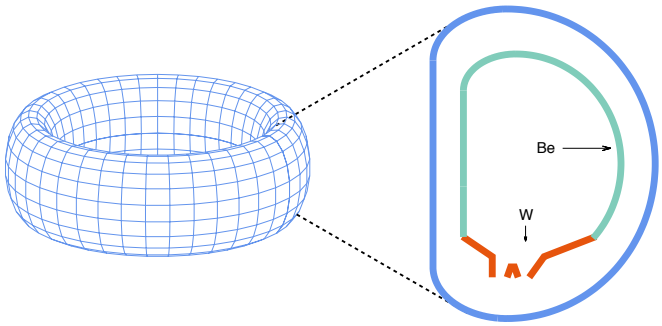

Figure 1.1: The cross-section of the torus-shaped vacuum vessel with the divertor illustrated in red in the bottom of the vacuum vessel.

The plasma facing material (PFM) of the divertor will have to withstand and lead away a substantial amount of heat and not having a mechanical failure when exposed to particle radiation from the plasma. In short, the desired material should have properties including

1. High melting point
2. High thermal conductivity
3. High resistance to particle radiation.

Tungsten is a material that has properties suitable as PFM in the divertor; it has the highest melting temperature among the metals, high thermal conductivity, low thermal expansion and also high resistance to particle radiation. Tungsten was selected as plasma facing material in the divertor in ITER [2] competing against carbon based materials. The divertor consists of three major parts: the inner and outer vertical target and the dome, which is the horizontal target. The tungsten thickness in the dome will be around 6 mm [1] while the tungsten thickness in the other areas will be considerably smaller [3]. The major part of the first wall in the vacuum chamber will be covered with Beryllium but some extremely exposed areas may be coated with tungsten.

ITER is currently under construction, with estimation of completion in 2019. ITER is not the end of the road and discussions about a demonstration power plant (DEMO) is underway. In DEMO, the operating conditions would be more extreme than in ITER and tungsten alone would not be suitable as PFM in the divertor. Because of this, compound materials based on tungsten are considered as candidates. Alloying tungsten with chromium could prevent oxidation by the same mechanism as in stainless steel, when chromium and oxygen form a passive layer which effectively slows down diffusion of oxygen. Besides chromium, yttrium is considered as alloying element, which has a stabilizing effect on the oxide formed. Both for ITER, and DEMO knowledge about thermodynamics and mechanisms of oxidation of tungsten is of prime importance for structural considerations in case the reactor is being exposed to oxidizing conditions.

Connected to its role in fusion power plants, tungsten and tungsten based alloys have applications as radiation shielding material in health care and the nuclear industry. It has a higher density than lead and many other common radiation shielding materials making it an efficient shielding material [4]. Due to the high cost of tungsten as opposed to lead, it is employed where there is limited space for shielding or in biological systems where lead cannot be used due to its negative effect on environment and health [5].

Tungsten readily forms oxides when exposed to conditions allowing oxidation, even at low temperatures and these oxides are interesting for a number of reasons.

The passive layers that are formed in stainless steel contain Cr_2O_3 which slows down oxygen transport through that layer and effectively hinders the formation of a iron oxygen phase. In stainless steels the chromium concentration is around 10% to obtain a fully passive layer. The effect of adding so much chromium to tungsten would have the adverse effect that the material would not be as resistant to sputtering by neutrons because of the relatively low mass of chromium. Therefore, it is desirable to design the tungsten material such that it becomes self passivating in that the tungsten oxide formed is a passive layer. Because of the operating conditions in a fusion reactor there will be transmutation of tungsten atoms to other elements. For safety reasons, the oxide that is formed should be dynamically stable so that radioactive elements are not spread in the atmosphere if the reactor were to be exposed to such conditions. That the oxide is dynamically unstable at a macroscopic scale is relatively common since the formation of an metal oxygen phase is usually accompanied by an increase in volume. The stability on a macroscopic level is a problem that is not addressed in this work. Tungsten oxides is naturally getting attention because the prominent role of W in fusion reactor design.

Tungsten oxides find use in other fields as well. WO_3 is an electrochromic material, which essentially means that the optical properties of the material can be reversibly altered by applying an electric field. This is utilized for example in smart windows that can control the amount of light that passes through.

Furthermore, in the last couple of decades gas sensors based on thin films of WO_3 has been developed [6, 7, 8] and is still an active field of research. Clearly, tungsten trioxide is an technologically important material, especially in energy related areas.

1.1.1 Aim and purpose

This work aims to clarify the structural properties of tungsten oxides and especially tungsten trioxide, since it is anticipated to be the most important oxide. From experimental and computational studies there are conflicting reports to as what crystal structures of tungsten trioxide that actually exists. In order to be able to assess the relative phase stability between the different phases of tungsten trioxide, the thermodynamical properties of tungsten trioxides is studied. This work also aims to provide an understanding about the oxidation process in tungsten and tungsten oxides from a point defect perspective. In order to study oxygen transport in tungsten oxides, it is necessary to first understand the thermodynamics of defects since defects are intimately connected to diffusion of atoms in a solid. The defect structure of material is generally very complex, specially when the defect concentration is high. The defect-defect interaction is beyond the scope of this work so the thermodynamics properties will strictly apply in the dilute limit of

concentration of defects. In this region formation and migration energies of defects can be obtained from thermodynamics of point defects.

Furthermore, this work aims to elucidate the role of extrinsic substitutional defects, such as yttrium on the dynamical stability of tungsten trioxide.

1.2 Background

1.2.1 Tungsten oxides

The crystal structure of W is body centered cubic (bcc) with lattice parameter 3.16 Å [9]. The electronic configuration of tungsten is $[Xe]5d^46s^2$, such that the most common oxidation state is +6. During oxidation, several different oxides forms, and the interesting concentration region, where most oxides of the form WO_x have been reported is in the interval $2 \leq x \leq 3$. The low oxygen concentration oxide tungsten(IV) oxide (WO_2) has a monoclinic structure with space group $P2_1/c$ but also an orthorhombic structure that is stable at high temperatures and high pressure. Between WO_2 and WO_3, the stoichiometric oxides $W_{18}O_{49}$, $W_{24}O_{68}$, W_nO_{3n-2} and finally W_nO_{3n-1} have been reported.

Tungsten(VI) oxide (WO_3), which is the more common oxide, is a polymorphic material with at least 9 different phases depending on temperature and synthesis path. In Figure 1.2 the crystal structure for monoclinic WO_3 with space group Pc is shown. The crystal structure consists of a network of WO_6-octahedra, in fact all phases of WO_3 has this general octahedra arrangement. In WO_3, the phases differ with respect to tilting pattern and deformation of the octahedron as well as the location of the center tungsten atoms in the octahedra. The crystal structure of monoclinic WO_2 with space group $P2_1/c$ also consists of WO_6-octahedra (Figure 1.3) but with the difference that the octahedra in WO_2 are edge-shared while they are corner-shared in WO_3. The symmetry and temperature range for each of the phases of WO_3 is found in Table 1.1.

When dealing with crystals, symmetry is an invaluable tool for characterizing structures and each crystal can be assigned to a space group which takes into account the translational symmetry of the Bravais lattice as well as the point symmetry group of the atoms in the crystal. There exist 230 space groups. Connected to symmetry is the notion of Wyckoff sites, which is a way of specifying where in a crystal the atoms sit.

While different phases have different symmetry, they share some key features too which allows one to study the low-temperature phases as proxies for the high-temperature phases. The reason for studying low-temperature phases instead of high-temperature phases is that the high-temperature phases are stabilized by temperature effects, which are not present in the theoretical framework that has

been used.

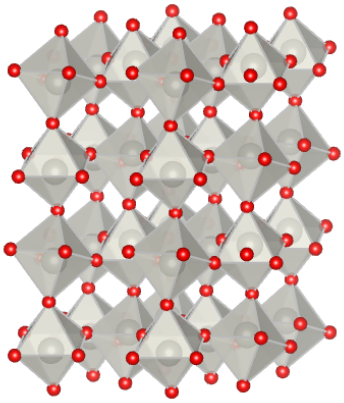

Figure 1.2: Octahedron arrangement in monoclinic WO_3 with space group Pc. The unit cell consists of 16 atoms and in the figure a 128 atom supercell is shown.

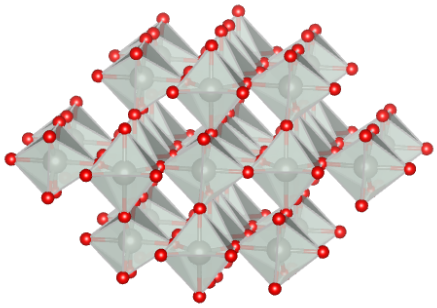

Figure 1.3: Octahedron arrangement for 96 atom monoclinic WO_2 supercell with space group $P2_1/c$. The unit cell consists of 12 atoms.

The general WO_3 structure can be seen as derivatives of a perovskite structure ABO_3 with a missing A atom, this can be seen in Figure 1.2. For perovskites there is a criterion based on the ionic radius of the involved atoms called the Goldsmith tolerance factor, which gives an indication of how the perovskite structure will look like. The Goldsmith tolerance factor is calculated as

$$t = \frac{r_{\mathrm{O}}}{\sqrt{2}(r_{\mathrm{W}} + r_{\mathrm{O}})}. \tag{1.1}$$

A value of the tolerance factor between 0.8 and 1.0 indicates that the involved atoms will form a cubic perovskite structure. The value of the tolerance factor for WO_3 is 0.3, which indicates that the cubic structure is not likely to be formed and experimentally the ideal cubic structure has never been observed.

Table 1.1: WO_3 structures. The acronym ITC refer to the *International Table of Crystallography* [10].

Space group	ITC no.	Structure	T[K]	Ref.
Pc	7	Monoclinic	< 220	[11]
$P\,\bar{1}$	2	Triclinic	< 290	[12]
$P2_1/n$	14	Monoclinic	< 740	[13]
$P2_1/c$	14	Monoclinic	300	[14]
$Pcnb$	60	Orthorhombic	< 950	[15]
$Pmnb$	62	Orthorhombic	< 950	[16]
$P\bar{4}2_1m$	113	Tetragonal	> 950	[17]
$P4/nmm$	129	Tetragonal	> 950	[18]
$P4/ncc$	130	Tetragonal	> 950	[15]
$P6/mmm$	191	Hexagonal	300	[19]
$P6_3/mcm$	193	Hexagonal	300	[20]

1.2.2 Lattice vibrations

Phonons are quantizations of lattice vibrations in solids and represented by normal modes. The structure of lattice vibrations in a general solid can be extremely complex because of the nature of the interaction between ions in a solid. Many concepts in solid state physics are readily described using the phonon concept, some of these include: thermal conduction and heat capacity, dynamical stability and elastic properties.

Phonons are also important for semiconductors in the process of recombination of electrons and holes. Furthermore, acoustic phonons close to Brillouin zone center are related to the elastic response of the material. Phonons provide a simple stability criterion for a crystal structure, namely that all frequencies in the Brillouin zone must be positive.

1.2.3 Defects

Introducing lattice imperfections such as point defects in an otherwise perfect lattice will increase the configurational entropy of the system which is given by Boltzmann formula: $S = k \ln W$, where W is a measure of the number of possible microstates resulting from the introduction of a defect. Because of this, crystals contain imperfections to some extent except at 0 K. The perfect lattice is in most cases the departing point for many models in solid state theory, but lattice defects are important since in many cases the thermal, electronic and elastic properties changes with the defect concentration. For example, in modern semiconductor

science, defects are introduced to change the charge carrier concentration, thus, alter the conducting properties of the material. Defects come in many types, zero-dimensional point defects to complicated multidimensional defects, such as cracks. Point defects, which are the type of defect that is considered in this work include self-interstitials, interstitials, substitutional atoms and vacancies. These types of defects are schematically illustrated in Figure 1.4. The interstitial, self-interstitial and vacancy defects in tungsten, and tungsten oxides influences the transport of oxygen in these materials. Therefore, it is very important to be able to characterize equilibrium concentrations of these defects, as well as the ability for the defect to move in the material.

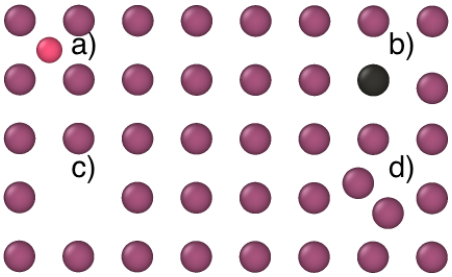

Figure 1.4: Different defects: a) interstitial, b) substitutional c) vacancy and d) split interstitial.

The most central property for describing the thermodynamics of a defect is the Gibbs free energy of formation

$$\Delta G_f = \Delta E_f + p\Delta V_f - T\Delta S_f, \tag{1.2}$$

however, in solids the pressure-volume term is usually small compared to the internal energy of the system and therefore neglected.

The formation energy ΔE_f describes the energy that has to be supplied in order to create a defect in a perfect lattice. The formation free energy is related to the concentration in the dilute limit for a system in thermal equilibrium. This relation is usually expressed as

$$c = c_0 \exp\left(-\frac{\Delta G_f}{k_b T}\right), \tag{1.3}$$

where c_0 is the concentration of available defect sites for this particular type of defect.

In tungsten trioxide, and in semiconductors in general, the presence of a band gap permits the formation of charged defects. This can be explained with tungsten trioxide as an example. Tungsten trioxide is an ionic material where tungsten has a formal charge state of $+6$ and oxygen -2. The oxygen atom has a formal charge

state of -2 since two electrons from the tungsten 5d orbitals are located in the $2p$ states of oxygen. To form a neutral vacancy, the two electrons from the $2p$ states of oxygen need to be transferred back to the tungsten $5d$ orbital before the oxygen atom is removed. Because of the band gap, it requires a substantial amount of energy to make this electron transaction and it could be energetically more favorable to remove the oxygen from the material together with the two surplus electrons.

1.2.3.1 Atomic transport in solids

Point defects can migrate in the material, which is connected to the oxidation of the material. Diffusion of atoms in solids are governed by microscopic jump processes.

The formation of oxides is governed by diffusion since the formation of tungsten oxide phases is dependent on oxygen concentration. In tungsten, oxygen atoms can be transported via interstitial diffusion or substitutional diffusion mediated by vacancies. In tungsten oxide, oxygen transport may occur by either interstitial or vacancy migration. Diffusion is governed by Ficks law:

$$\partial_t c = \nabla(D\nabla c) \tag{1.4}$$

where D is the diffusion coefficient, which can often be described by the Arrhenius form:

$$D = D_0 \exp\left(-\frac{E_a}{k_b T}\right). \tag{1.5}$$

D_0 is related to the attempt frequency and lattice geometry, and the exponential term governs the probability of success. The pre factor D_0 in equation (1.5) can be obtained by calculating the vibrational frequencies of the system [21]. The activation energy E_a is a measure of the energy barrier that needs to be climbed and for atomistic motion in solids it is usually referred to migration energy and is on the order of 0.1-1 eV. The diffusion coefficient D is related to the mean squared displacement (MSD)

$$\text{MSD} = 6Dt \tag{1.6}$$

where t is the time. The mean squared displacement is a measure of how much the particle deviates from the average position and the square root of the MSD gives the average displacement distance at a specific time. The relation between the diffusion coefficient and the MSD is based on a single atom random walk.

2 Method

The calculations in this work have been performed within density functional theory and in this section a brief description of the method and some of the relevant limitations and problems are presented.

2.1 Density functional theory

Density functional theory (DFT) is essentially a method for solving the time independent Schrödinger equation. Is is based on the ground state electron density instead of the wave functions, which many other methods use such as Hartree-Fock and Green's function methods. DFT effectively reduces the number of independent variables of the system under consideration, which reduces the computational cost significantly. DFT, like most methods, departs from the many electron stationary Schrödinger equation $\hat{H}\Psi = E\Psi$ written in atomic units within the Born-Oppenheimer approximation, where $\hat{H}$ is

$$\hat{H} = -\frac{1}{2}\sum_i \nabla_i^2 + \sum_{i,l} \frac{Z}{|r_i - r_l|} + \frac{1}{2}\sum_{i \neq j} \frac{1}{|r_i - r_j|}, \tag{2.1}$$

where the index i and j runs over the electrons and l runs over the ions. The first term is the kinetic energy operator $\hat{T}$ and the second is the electrostatic potential due to ions and is called the external potential operator: $\hat{V}_{\text{ext}}$. The last term in equation (2.1) couples electrons to each other, effectively making this a many body problem, which is very difficult to solve exactly.

2.1.1 Hohenberg-Kohn theorems

In 1964 Hohenberg and Kohn published a seminal paper [22] which concludes that there exists a one to one correspondence between ground state wave function and ground state electron density. To be more specific the first Hohenberg-Kohn theorem states that the ground state energy (or external potential) is determined uniquely by the electron density.

The first Hohenberg-Kohn theorem is not constructive in the sense that it does not offer a method to find the electron density. The second Hohenberg-Kohn theorem asserts that $E[n_0] \leq E[n_1]$ whenever n_1 is not the ground state electron density, and since

$$E[n] = T[n] + U_H[n] + V_{\text{ext}}[n] \tag{2.2}$$

the ground state electron density can be found by minimizing the energy functional in equation (2.2).

2.1.2 Kohn-Sham equations

Kohn and Sham proposed [23] to replace the many body problem as described by equation (2.2) with an artificial independent electron problem effectively changing the potential. The Kohn-Sham energy is written as

$$E[n] = T_s[n] + V[n] + U_H[n] + V_{\mathrm{XC}}[n]. \tag{2.3}$$

This is still a many body problem, exact and equivalent to equation (2.1) but the exchange and correlation energy has been collected in V_{XC}. The exchange energy comes from the antisymmetry principle for fermions and the correlation from that the electrons are not independent of each other. By applying the variational principle the Kohn-Sham equations are obtained [24]

$$\left(-\frac{1}{2}\nabla^2 + V_{\mathrm{ext}}(r) + V_{\mathrm{Hartree}}(r) + V_{\mathrm{XC}}(r) - \varepsilon_i \right)\psi_i(r) = 0. \tag{2.4}$$

2.1.3 Exchange-correlation functionals

Equation (2.4) is still containing the potential associated with exchange and correlation. The exchange-correlation energy can be approximated with the local electron density approximation (LDA), where the exchange-correlation potential is approximated by the potential of a homogenous electron gas of the same density [25].

This is the simplest approximation and rarely used in modern calculations, it can, however, be extended to the so called generalized gradient approximation (GGA), which are the class of functionals mainly used in this work. In GGA functionals the spatial variation of the electron density is also taken into account, in a way reminiscent of a Taylor expansion. This makes functionals from the GGA class more accurate, specially in cases where the electron density vary rapidly [25]. LDA is a local functional and GGA-type functionals are semi-local, in the sense that the exchange-correlation potential can be written as

$$V_{\mathrm{XC}} = \int f(n(r), \nabla n(r)) dr. \tag{2.5}$$

Functionals from the GGA class comes in different parameterizations and some of the more well-known are PBE [26], PBEsol[27], which has been utilized in this work. The PBE functional is probably the most common and PBEsol and is a

variation of it, optimized for solids. There exists extensions to GGA-type functionals such as meta-GGA functionals such as AM05 [28]. Functionals that are constructed solely via local quantities cannot describe dispersive interactions, such as van der Waals (vdW) interaction, and recent developments have resulted in a vdW class of functionals, which essentially extends semi-local GGA with nonlocal interactions. van der Waals type functionals have received a lot of attention because of the new possibilities a fully working description of vdW interaction opens up. This interaction is important in biochemical and soft materials systems. An example of a vdW class functional is the vdW-DF-CX functional developed at Chalmers [29].

It is well known that many exchange-correlation functionals have problems in describing the band gap in semiconductors and insulators. There is a tendency to underestimate the band gap. Hartree-Fock, which is a wave function based method tends to overestimate the band gap and by modifying the exchange-correlation functional as to include some of the exact exchange energy that is present in Hartree-Fock so called hybrid functionals are obtained. In this work the hybrid functional HSE06 [30] has been used.

3 Computational details

The projector augmented wave (PAW) method as implemented in *Vienna ab initio simulation package* [31, 32, 33, 34] (VASP) has been used for all DFT calculations. Throughout the whole work PAW-potentials with s2p4 electrons in oxygen and 6s5d electrons in tungsten were used. For yttrium the 4s4p5s4d electrons were treated as valence electrons.

3.1 Relaxation

The experimental crystal structures as found in Table 1.1 in the background section has been used as the departing point for ionic relaxation. For metallic materials a Methfessel-Paxton scheme with smearing parameter 0.2 eV was used and for the band gap materials a Gaussian smearing with the same smearing parameter was used. For the band gap materials no energy difference was observed while varying the smearing parameter while for metals a slight energy difference could be observed. For computational and convergence reasons the parameter was set to 0.2 eV.

The cohesive energy of oxygen was obtained by making a Γ-point spin polarized calculation of an oxygen dimer molecule. The vdW-DF-CX functional does not have a rigorous theoretical implementation of spin polarization in VASP, however, there is a less rigorous implementation that gives very similar results as PBE for spin polarization compared with non spin polarized calculations.

For most relaxation computations, all internal parameters (ionic position, shape and volume of cell) were allowed to relax. For the oxygen dimer calculation the volume of the cell was held constant to simulate an oxygen dimer and not a bulk structure. Carrying out volume relaxation, the basis set changes with size of the unit cell since specifying the plane wave cutoff energy effectively singles out the plane waves with wave vector k satisfying

$$\frac{|k-G|^2}{2m_e} < E_{\text{cutoff}}. \tag{3.1}$$

Therefore, convergence was confirmed by restarting the calculations until no ion position changed. For the structural calculations, three different GGA-type exchange-correlation functionals was used: PBE [26], PBEsol [27], vdW-DF-CX [29] and one meta-GGA: AM05 [28]. For some structures the HSE06 functional [30] was also used. The reason for using several exchange-correlation functionals was to study

which functionals that described the system in the most accurate way. The structures were allowed to relax until the maximal force on any ion in the system was lower than 5 meV/Å.

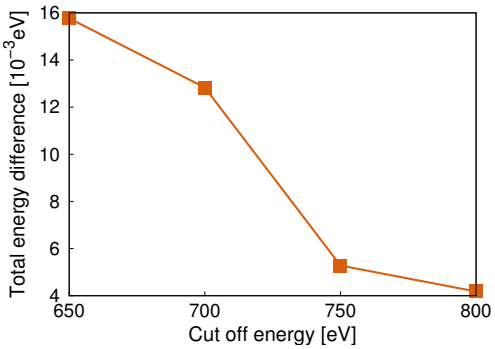

Figure 3.1: Convergence of total energy with respect to plane wave cutoff energy computed for k-spacing of 0.2 Å^{-1} for monoclinic WO_3 in space group P_21/c. The total energy difference is between successive parameter settings, which are 50 eV apart in all cases.

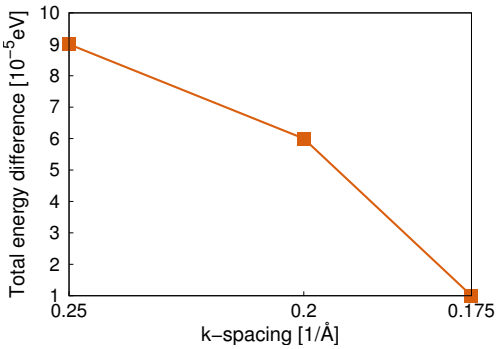

Figure 3.2: Convergence with respect to k-spacing computed with 700 eV plane wave cutoff energy for monoclinic WO_3 in space group P_21/c. The total energy difference is between successive parameter settings. The first point is the difference in total energy between 0.3 Å^{-1} and 0.25 Å^{-1}

.

3.2 Phonons

There are various ways to calculate the vibrational properties of a solid, such as molecular dynamics and correlation function approaches, linear response and purely force based calculations based on supercells, which is the method used in this work.

The method is implemented in the `phonopy` software [35] and is described as follows with the notation used in `phonopy`. The method departs from the series expansion of the potential energy of the atoms to the second order which corresponds to the harmonic approximation. The first order term is zero by the assumption that the system is at equilibrium. Potential energy and force are related as

$$\Phi_{\alpha\beta}(jl, j'l') = \frac{\partial^2 E}{\partial r_\alpha(jl)\partial r_\beta(j'l')} = -\frac{\partial F_\beta(j'l')}{\partial r_\alpha(jl)}, \tag{3.2}$$

where $\Phi_{\alpha\beta}$ is the second order force constant, α and β are Cartesian directions and j, j', l, l' are particle and unit cell indeces. The force constant matrix is calculated

by a finite difference of the derivative as

$$\Phi_{\alpha\beta} \approx \frac{\Delta F_\beta(j'l')}{\Delta r_\alpha(jl)}, \tag{3.3}$$

where the ΔF_β are calculated by DFT after displacing the atoms by a small distance. The standard way of obtaining the lattice dynamics from the force constants is to form the so called *dynamical matrix* with elements

$$D_{\alpha\beta}(jj', q) = \frac{1}{\sqrt{m_j m_{j'}}} \sum_{l'} \Phi_{\alpha\beta}(j0, j'l') \exp(iq \cdot [r(j'l') - r(j0)]). \tag{3.4}$$

This matrix can be used to formulate an eigenvalue problem

$$D(q)e_q = \omega_q^2 e_q, \tag{3.5}$$

where ω_q is the vibrational frequency and e_q is the eigenvector of displacements of the normal mode. For each q there is a set of eigenvalues ω_q^2 that makes up the phonon dispersion relation $\omega(q)$. To calculate the phonon frequencies at the zone center, only the unit cell is needed, while in order to resolve zone boundary modes a supercell consisting of at least two unit cells in that direction is needed. The fact that WO_3 generally possesses large unit cells and low symmetry sets limits to what calculations can be performed with a reasonable cost, so the full dispersion was not studied for all structures. The phonon dispersion has to be accurately calculated in order to avoid imaginary frequencies.

In Appendix B, the result of a convergence study for different parameter settings can be found. From this, the main conclusion is to avoid using real space projectors. Furthermore, the basis set should be kept as big as possible. The energy convergence criterion in the self consistent loop on the other hand is having little effect below 10^{-4} eV, except for requiring substantially more computation time.

3.3 Defects

When calculating defect formation energies, the ideal system is modified to host one or more defects of the types described in Section 1.2.3. In order to maintain a low defect concentration and small image interaction, supercells are used. In the supercell formalism the formation energy of a point defect in a material is given by

$$\Delta H_f = E_{\text{def}} - E_{\text{ideal}} - \sum_i n_i \mu_i + q\varepsilon_{VBM} + q\Delta\mu_e + qV_{\text{align}} + E_{\text{corr}}, \tag{3.6}$$

where E_{def} is the defect host system, E_{ref} is the ideal host. E_{corr} represents the correction for periodic image interaction. The μ_i is the chemical potential of species i and is used to model the conditions for defect formation. The sign of n_i is positive if species i is added, and vice versa. In a band gap material the term $\varepsilon_{VBM} + \mu_e$ is the chemical potential of electrons.

3.3.1 Energy corrections

Calculating formation energy for charge neutral defects, the main consideration to get accurate result is to use large enough supercell so that the defect interaction by local perturbations in the electron density vanish. When the defects are charged, long range Coulomb interactions which generally do not decay rapidly, become important. The following main difficulties arise when considering charged defects:

1. Image charge interactions.
2. Different reference energies between ideal and defect system.
3. Electron chemical potential depends on band gap which is poorly described within DFT.

Below the approaches to solve the problems are described.

3.3.1.1 Image charge correction

Because of the relatively large values of entries in the dielectric tensor (seen in Appendix C) for tungsten trioxide the image charge interaction is anticipated to be strongly screened. The Coulomb interaction scale quadratically with the charge state, which means that even relatively small values for the image charge correction may provide a significant contribution to the formation energy of a defect.

The interaction energy between two charges therefore rapidly decreases with distance, but since small values for the image charge interaction may still play a significant role for formation energies for defects with large charge states corrections are necessary. Makov and Payne proposed [36] an image charge correction based on a multipole expansion of the defect charge density

$$E_{\text{MP}} = \frac{q^2\alpha}{2\varepsilon L} - \frac{2\pi qQ}{3\varepsilon\Omega}, \tag{3.7}$$

where α is the Mandelung constant, ε is the dielectric tensor, Q is the quadrupole moment of the charge and Ω is the supercell volume. Lany and Zunger later proposed [37] a simplified expression for the total correction, expressed in terms of the first term on the RHS in equation (3.7)

$$E_{\text{corr}} = (1 + f(1 - \varepsilon^{-1}))\frac{q^2\alpha}{2\varepsilon L}, \tag{3.8}$$

where f is a form factor which has been calculated for cubic systems and has a value close to $-1/3$. The smallest value in the diagonal elements of the dielectric tensor is on the order of ~ 10 which makes the form factor multiplied by the inverse of the dielectric constant small and as an approximation the simplified form of equation (3.7) is used to correct for image charge interactions.

The dielectric function is calculated with density functional perturbation theory, which is implemented in VASP. The correction term is then calculated with the General Utility Lattice Program (GULP) [38].

The unit cells in ground state WO_2 and WO_3 are non-cubic but since defects require large defect separations in terms of periodic images, supercells that are as cubic as possible are constructed and the shape factor for the cubic system can then be used.

To obtain as cubic supercell as possible a combinatorial method to minimize the non-cubic effects has been developed [39]. The method involves the construction of an integer matrix P that multiplies the cell metric h of the non-cubic system. From Ph the volume of the cell: Ω is easily obtained, and the corresponding cubic cell metric is found as $\Omega^{-1/3}I$, where I is the identity matrix. By sweeping over all such matrices P and minimizing the difference between non-cubic cell metric and cubic cell metric, the most cubic choice of P for each volume is found, which can be put in correspondence with the number of atoms in the supercell. The result is presented for tungsten oxides in Figure 3.3. Care has been taken to make calculations on as cubic supercells as possible.

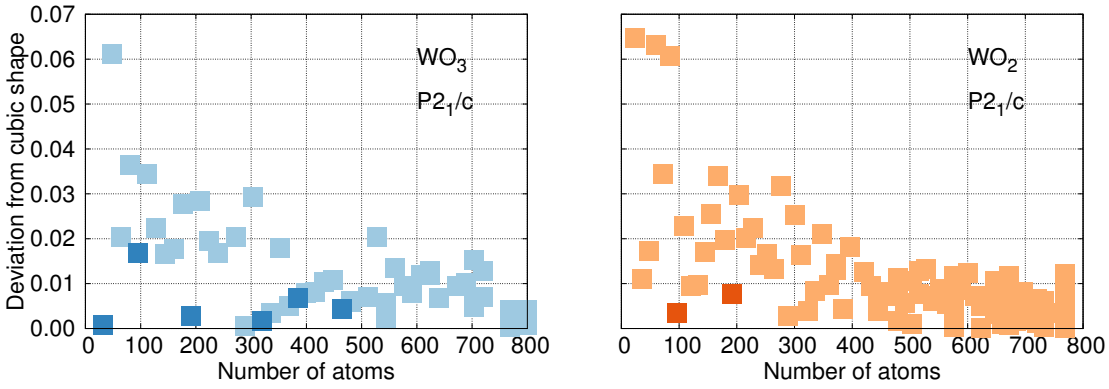

Figure 3.3: Deviation from cubic shape for WO_2 and WO_3. The dark colors indicate structures that have been used for defect calculations.

3.3.1.2 Potential alignment

The charge distribution within a supercell generates a electrostatic potential of the form

$$U(r) = \int \frac{n(\tilde{r})}{|r - \tilde{r}|} d\tilde{r}. \tag{3.9}$$

U is called the Hartree potential and conventions of DFT codes is to set the average of U to zero. When a defect is introduced in the system, it will perturb the local electron density but the bulk properties should, sufficiently far from the defect center, not be affected. The consequence of setting the average of U to zero is that bulk-like regions in defect and ideal supercell, which should have similar properties, differ in the average electrostatic potential.

Because of this, the Hartree potential has to be aligned between ideal and defect systems in order to be able to compare energies, this is the qV_{align} term in equation 3.6. V_{align} is calculated by considering the average electrostatic potential at each ion in the supercell for both ideal and neutral defect systems and calculate the difference at the ion furthest away from the defect center.

The difference in average electrostatic energy varies, as can be seen for a typical case in Figure 3.4, therefore, the potential alignment has been calculated by averaging over the 10 values of atoms furthest from the defect center to better capture the asymptotic behavior. In Figure 3.4 there is a deviation from the expected behavior between 5 Å and 6 Å for some oxygen atoms, this behavior is not present in a PBE calculation of the average electrostatic potential.

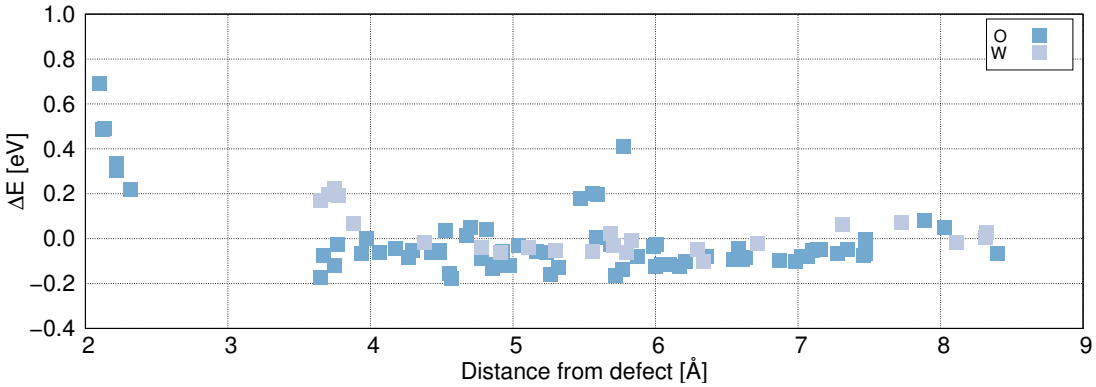

Figure 3.4: The difference in average electrostatic potential between ideal and defect supercell for substitutional Y in 96 atom supercell of WO_3 with space group $P2_1/c$ calculated with the vdW-DF-CX functional.

3.3.2 Chemical potential

In equation (3.6) the expression $n_i\mu_i$ has to be evaluated, where $\mu_i = \frac{\partial G}{\partial n_i}$ is the chemical potential of atom species i. The chemical potential can be broken into two terms

$$\mu_i = \mu_i^\circ + \Delta\mu_i, \tag{3.10}$$

where μ_i is the chemical potential of atom species i in its most stable form, $\Delta\mu_i$ is related to the reference state of the atom species i. In the case of compounds which we will be interested in, the formation energy and change in chemical potential are related according to

$$H_f(\mathrm{A}_m\mathrm{B}_n) = m\Delta\mu_\mathrm{A} + n\Delta\mu_\mathrm{B} \tag{3.11}$$

and by specifying the conditions, at which the formation of the compound takes place, the limiting conditions are either A-rich or B-rich. In the A-rich limit the formation energy of the compound is not coupled to the change in energy with respect to the number of A atoms, and hence $H_f(\mathrm{A}_m\mathrm{B}_n) = n\Delta\mu_\mathrm{B}$. In the same way, in the B-rich limit the heat of formation and chemical potentials is related as $H_f(\mathrm{A}_m\mathrm{B}_n) = m\Delta\mu_\mathrm{A}$. Accordingly, the change in chemical potential can be determined with respect to different states. The standard chemical potential of the compound in the elemental form is μ_i°, and is taken as the opposite of the cohesive energy of the element. Specifically in the case of oxygen, there is a wide variety in the literature on how to treat μ_i for oxygen. Some studies refer to the solid form, while others refer to it in dimer form and some use experimental values. In this work, the energy has been calculated as half the oxygen dimer energy.

Furthermore, there are thermodynamical boundary conditions that needs to be taken into consideration, which are formulated in equation (3.12) and illustrated in Figure 3.5.

$$\begin{aligned} \Delta\mu_\mathrm{W} + 3\Delta\mu_\mathrm{O} &\leq \Delta H_f(\mathrm{WO}_3) \\ \Delta\mu_\mathrm{W} + 2\Delta\mu_\mathrm{O} &\leq \Delta H_f(\mathrm{WO}_2) \end{aligned} \tag{3.12}$$

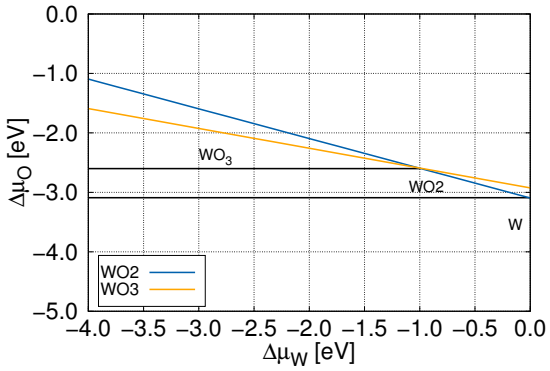

Figure 3.5: The relation between the relative chemical potential of oxygen and the relative chemical potential of tungsten for monoclinic WO_2 and WO_3, both in space group $P2_1/c$.

3.3.3 Defect clustering

The strength of defect-defect interactions can be expressed in terms of the binding energy, which for example for oxygen vacancies is defined as

$$\Delta E_{\text{O-O}} = \Delta E_f(2V_{\text{O}}) - 2\Delta E_f(V_{\text{O}}) = E_{\text{def}}(2V_{\text{O}}) + E_{\text{id}} - 2E_{\text{def}}(V_{\text{O}}). \tag{3.13}$$

3.3.4 Yttrium defects

Yttria (Y_2O_3) is used to form so called yttria stabilized zirconia (YSZ) by substituting a Zr^{+4} ion with a Y^{+3} ion to form a charged substitutional defect. This charge has to be compensated for in some way which is usually accompanied by the formation of defects.

Yttria has a stabilizing effect on ZrO_2 in terms of mechanical strength and crystal structure. Because of this, the substitutional formation of Y from yttria is studied in order to determine wether the dynamical stability of WO_3 can be enhanced by a similar mechanism. The formation energy for the yttrium substitutional defect is

$$\begin{aligned} E_f =& E_{\text{def}} - E_{\text{ideal}} + q(\varepsilon_{\text{VBM}} + \Delta\mu_e + V_{\text{align}}) - E_{\text{Y}}^{\text{HCP}} \\ & - \frac{1}{2}\Delta H_f(\text{Y}_2\text{O}_3) + E_{\text{W}}^{\text{BCC}} + \Delta H_f(\text{WO}_3) + \frac{2}{3}E_{\text{MP}}, \end{aligned} \tag{3.14}$$

where the chemical potential for Y in the oxygen rich limit is

$$\mu_{\text{Y}} = E_{\text{Y}}^{\text{HCP}} + \frac{1}{2}\Delta H_f(\text{Y}_2\text{O}_3). \tag{3.15}$$

In this expression, the cohesive energy for Y is calculated in the most stable hexagonal close packed structure.

4 Tungsten

In this section properties for tungsten are reported. These properties are also important for calculation of the formation energies of tungsten oxides. Formation and migration energies are calculated, which are of interest to understanding the oxidation process in tungsten.

4.1 Structure

In Table 4.1 cohesive energies and lattice parameters are compiled for different exchange-correlation functionals. Clearly, vdW-DF-CX performs better when comparing lattice parameter with experimental values but the cohesive energy is better described with PBE and PBEsol. The lattice parameter described by PBE is more accurate than the one described with PBEsol while the cohesive energy calculated with PBEsol is slightly more in agreement with the experimental value than the cohesive energy for calculated with PBE.

Table 4.1: Total energy for W in bcc structure, atomic energy for W, cohesive energy for bcc W and lattice parameter for different exchange-correlation functionals. Experimental cohesive energy is extrapolated to 0 K and atmospheric pressure while the experimental lattice parameter is measured at room temperature.

	$E_{\text{tot}}^{\text{bcc}}$ [eV]	E_{atom} [eV]	E_{coh} [eV]	a [Å]
vdW-DF-CX	−11.25	−1.85	−9.40	3.154
PBE	−13.02	−4.54	−8.48	3.172
PBEsol	−13.88	−4.61	−9.27	3.145
AM05	−13.66	−2.55	−11.11	3.138
Exp. [9]			−8.9	3.16

4.2 Defects

4.2.1 Individual defects

Table 4.2: Defect formation energies in tungsten from a 128 atom supercell. The chemical potential of oxygen is $1/2E[O_2]$ and the chemical potential of W is total energy of one W atom in bcc.

	This work		Other calculation
	vdW-DF-CX	PBE	
V_W	4.26	3.24	3.27 [40]
O_i	0.20	0.24	−1.73 [41]

The formation energy of the tungsten vacancy calculated with vdW-DF-CX is higher than the PBE value of 3.27 eV, which agrees well with values found in [40]. The vdW-DF-CX value, however, is a bit higher than the experimental value of 3.60±0.2 eV [42]. Oxygen impurities in tungsten are likely to be in the form of interstitials because of the relative big difference in size between tungsten and oxygen atoms. Therefore, calculations of oxygen substitutional defects were omitted. Tungsten vacancies might create environments suitable for oxygen trapping by opening up space in the structure.

The formation energy for an oxygen interstitial in the tetrahedal interstitial site (TIS) is 0.20 eV, which means that oxygen interstitials are rare at low temperatures. Regarding the interstitial formation energy there is a significant discrepancy, both in magnitude and sign compared to other calculations with PW91 [41], a functional that has not been considered in this work. The vdW-DF-CX and PBE values for the oxygen interstitial formation energy calculated in this work are quite similar. It should be noted that the O_i formation energies in Table 4.2 has been calculated in the O-rich limit, with $\mu_O = \frac{1}{2}E_{tot}(O_2)$. Oxygen gas serves as an ideal reservoir for oxygen but it is probably not the most correct reference state since it is possible that the oxygen reservoir is WO_2. This situation is illustrated in Figure 3.5. The formation energy of an oxygen interstitial rises to 3.49 eV with WO_2 in space group $P2_1/c$ as the oxygen reservoir. Tungsten does not form suboxides (oxides with very low oxygen concentration) and the large formation energy of an oxygen interstitial may be a manifest of this property. With the formation energy, the solubility in the dilute limit can be estimated by equation (1.3) at a specific temperature. The concentration of oxygen interstitials at room temperature and WO_2 as the oxygen reservoir is 8.88×10^{-36} interstitials/cm^3, which means that it is an extremely low probability to find oxygen interstitials in tungsten. If the

oxygen reservoir is oxygen gas, then the concentration of oxygen interstitials at room temperature is 7.25×10^{16} interstitials/cm^3. The tungsten vacancies were calculated with $\mu_{\mathrm{W}} = E_{\mathrm{W}}^{\mathrm{BCC}}$.

The TIS is located on $a[\frac{1}{2}\frac{1}{4}0]$ equivalent positions, and some of the positions can be seen in Figure 4.1. The TIS is energetically favorable over the octahedral interstitial site (OIS), which is located halfway between site 1 and 3 in Figure 4.1. The difference in energy between TIS and OIS is approximately 0.30 eV, which can be seen in Figure 4.2, and the barrier heights are consistent with results in [41]. Compared with $k_B T$ at room temperature, which is around 0.025 eV, migration of oxygen interstitial requires relatively high temperatures to be frequent.

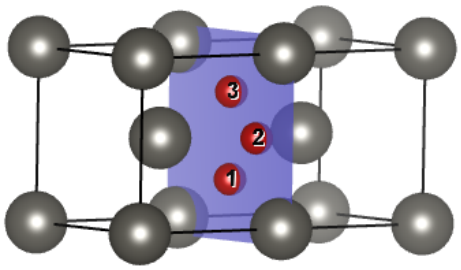

Figure 4.1: Tetrahedal interstitial positions for oxygen in tungsten.

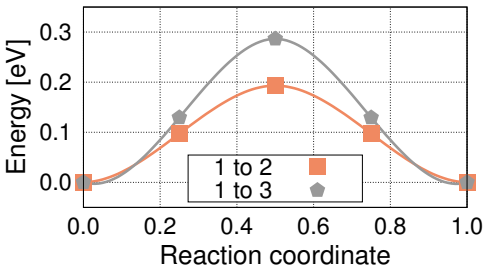

Figure 4.2: Migration energy for oxygen interstitial in tungsten.

The prefactor D_0 in equation (1.5) can be estimated as $\nu_0 \alpha^2$, where ν_o is an effective frequency of the system which is assumed to be 1 THz and α is the length between interstitial sites. The estimated diffusion coefficient for interstitial oxygen diffusion in tungsten at room temperature is then 1.39×10^{-6} cm^2/s. The square root of the MSD is shown in Figure 4.3 for a range of temperatures. The range of temperatures is expected to cover the operating temperature at the wall, which is estimated to fall in the range of 800 K to 1500 K depending on location [1]. In some parts of the fusion reactor, a tungsten coating with a thickness of 10-20 μm will be used [3]. The high MSD at elevated temperatures suggests that oxygen will migrate though the tungsten coating very rapidly. The bulk W divertor is almost 6 mm thick [1], which means that most of the divertor would be unaffected by the oxygen atmosphere.

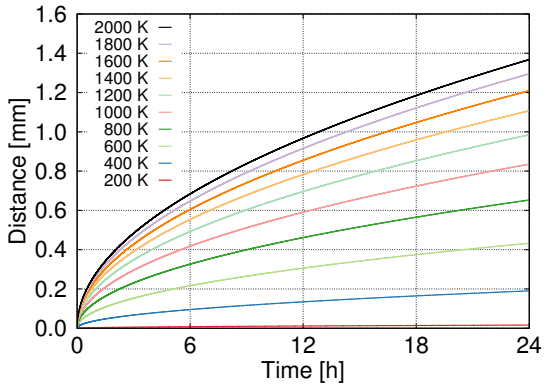

Figure 4.3: The square root of the MSD of oxygen interstitial in tungsten as a function of time for temperatures in the interval 200 K to 2000 K.

4.2.2 Defect clustering

The interaction of was investigated as a function of the oxygen distance has been conducted, with the result presented in Figure 4.4. It is apparent that oxygen are attached to each other. The resulting defect cluster are likely to play a role in the formation of oxide nuclei.

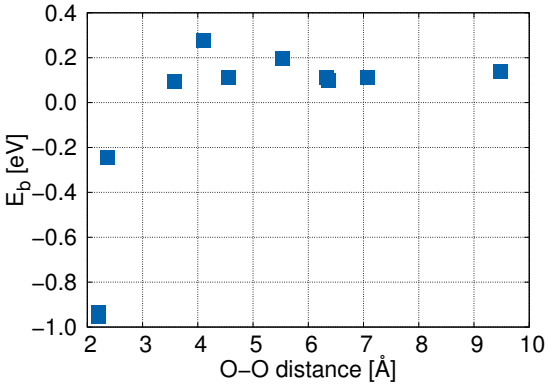

Figure 4.4: Oxygen-oxygen interaction in tungsten.

The shortest O-O distance in W is 2.20 Å corresponding to an interaction energy of close to −1.00 eV. The bond length in the oxygen dimer calculated with vdW-DF-CX is 1.22 Å, which means that it is unlikely that the large interaction energy is a result of pure oxygen-oxygen bond formation. The negative binding energy, at least partly, is a result of elastic effects. It is possible to construct larger oxygen clusters by adding more oxygen atoms close to each other. This is shown in Figures 4.5-4.7 with the corresponding charge density in Figure 4.8-4.10. After

relaxation, the oxygen configuration is planar, all oxygen sits in the same plane instead of adopting a 3-dimensional configuration.

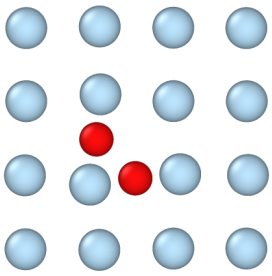

Figure 4.5: 2 interstitials in tungsten.

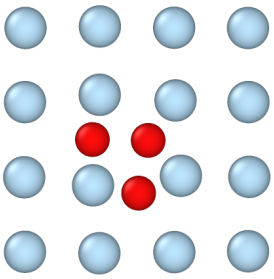

Figure 4.6: 3 interstitials in tungsten.

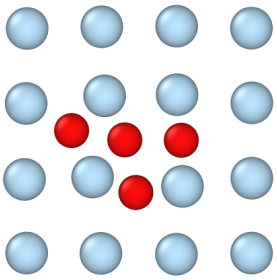

Figure 4.7: 4 interstitials in tungsten.

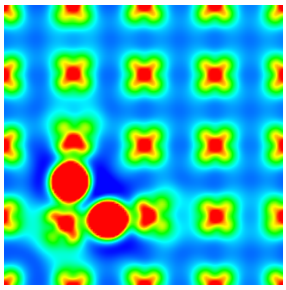

Figure 4.8: 2 interstitials in tungsten.

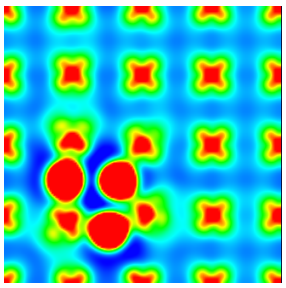

Figure 4.9: 3 interstitials in tungsten.

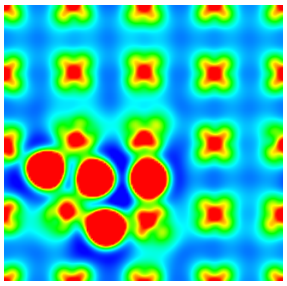

Figure 4.10: 4 interstitials in tungsten.

The effect of placing two oxygen interstitials at a short distance from each other is that the charge density of the adjacent tungsten atom is rearranged. There is a charge density increase consistent with a covalent bond formation between the adjacent tungsten atom and the two tungsten atoms located closest to it. The charge density rearrangement that is present for the two oxygen atoms located close to each other is not present when the distance between the oxygen atoms is getting longer.

5 Tungsten dioxide

This section begins with results concerning structural and vibrational properties. After which the electronic band structures are presented. Initial investigations of the defect properties are presented for the monoclinic structure. The last part of this section contains the result obtained from calculations on yttrium doped tungsten dioxide.

5.1 Structure

The monoclinic WO_2 is the more common structure and the structure is described in Figure 5.1. The unit cell for the monoclinic structure consists of 12 atoms, but only two of the eight oxygen are unique and all tungsten sites are equivalent. The blue plane is a mirror symmetry plane. The yellow plane contains oxygen atoms located in one unique position, another set of sites of the same unique oxygen positions is located parallel to the yellow plane, but displaced along the intersection of the blue and yellow plane. The general arrangement of the oxygen sites in monoclinic WO_2 can be interpreted as two atom thick-layers placed after each other in a repetitive manner. Tungsten-oxygen distances for both the monoclinic and orthorhombic structure can be found in Table 5.4. The tungsten dioxide crystal structures are well described within DFT. The lattice parameters are compiled in Table 5.1 for monoclinic WO_2 in space group $P2_1/c$ and in Table 5.2 for the orthorhombic structure in space group *Pnma*. vdW-DF-CX describes the lattice parameters and angles in both structures well compared with experimental data. The difference between the different functionals is generally small. PBEsol and AM05 describes very similar parameters and angles for both systems while PBE overestimates the lattice parameters and angles. PBE predicts the angle in the monoclinic WO_2 to be around 5° off from experimental data, which in contrast with the other functionals is a large error. The cohesive energies calculated with the different exchange-correlation functionals are compiled in Table 5.3. All functionals predicts a more negative cohesive energy for the orthorhombic structure than for the monoclinic structure.

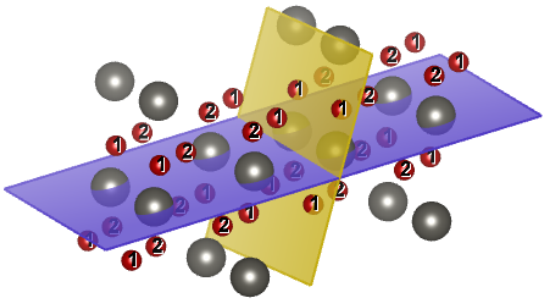

Figure 5.1: Crystal structure for monoclinic WO_2 with space group $P2_1/c$. The yellow plane contains oxygen sites located on Wyckoff 4e sites.

Table 5.1: Structural properties for monoclinic WO_2 with space group $P2_1/c$ calculated with different exchange-correlation functionals. The unit cell consists of 12 atoms where the oxygen atoms occupy two different Wyckoff 4e sites and the tungsten atoms occupy Wyckoff 4e sites. The experiment for $P2_1/c$ has been carried out in room temperature.

	a [Å]	b [Å]	c [Å]	α [°]	β [°]	γ [°]
vdW-DF-CX	5.550	4.918	5.675	90	120.472	90
PBE	5.583	4.943	5.711	90	125.801	90
PBEsol	5.527	4.905	5.662	90	120.370	90
AM05	5.520	4.904	5.660	90	120.407	90
Exp. [43]	5.577	4.899	5.664	90	120.678	90

Table 5.2: Structural properties and bond lengths for orthorhombic WO_2 with space group $Pnma$ calculated with different exchange-correlation functionals. The unit cell has 36 atoms and there are 4 unique oxygen sites, two of which are Wyckoff 8d sites and two Wyckoff 4c sites. The tungsten atoms occupy the Wyckoff 8d and 4d sites. The experiment for $Pnma$ was carried out at 1120 K and 80 kbar.

	a [Å]	b [Å]	c [Å]	α [°]	β [°]	γ [°]
vdW-DF-CX	9.702	8.447	4.769	90	90	90
PBE	9.748	8.488	4.841	90	90	90
PBEsol	9.666	8.419	4.776	90	90	90
AM05	9.651	8.407	4.792	90	90	90
Exp. [44]	9.716	8.438	4.756	90	90	90

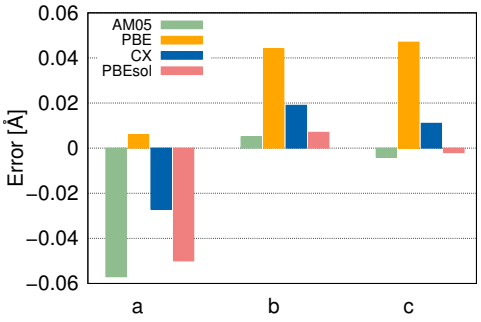

Figure 5.2: Error for different exchange-corrrelation functionals in lattice parameter and angels for monoclinic WO_2 with space group $P2_1/c$.

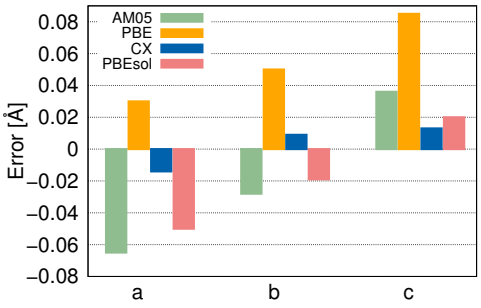

Figure 5.3: Error for different exchange-corrrelation functionals in lattice parameter and angels for orthorhombic WO_2 with space group $Pnma$.

Table 5.3: Cohesive energies in eV/f.u for both phases of WO_2 calculated with different exchange-correlation functionals.

Space group	vdW-DF-CX	PBE	PBEsol
$P2_1/c$	−24.802	−21.012	−22.459
$Pnma$	−24.831	−21.018	−22.476

Table 5.4: W-O bond lengths in WO_2-structures in Å.

$P2_1/c$		$Pnma$		
Direction	W 4e	Direction	W 8d	W 4c
$\langle\bar{1}1\bar{1}\rangle$	2.00	$\langle1\bar{1}1\rangle$	2.04	2.01
$\langle11\bar{1}\rangle$	2.08	$\langle10\bar{1}\rangle$	2.11	2.06
$\langle011\rangle$	2.00	$\langle\bar{1}1\bar{1}\rangle$	2.01	2.04
$\langle0\bar{1}\bar{1}\rangle$	1.97	$\langle\bar{1}01\rangle$	2.06	2.11
$\langle\bar{1}\bar{1}0\rangle$	2.01	$\langle111\rangle$	2.04	2.01
$\langle1\bar{1}1\rangle$	2.08	$\langle\bar{1}\bar{1}\bar{1}\rangle$	2.01	2.04

The smallest W-W distance is 3.08 Å in monoclinic WO_2 in space group $P2_1/c$ while the smallest distance in the orthorhombic structure is 2.57 Å. The formation energy calculated with vdW-DF-CX of WO_2 in space group $P2_1/c$ is -6.19 eV per formula unit to be compared with the experimental value of -6.11 eV per formula unit [45]. The formation energy for WO_2 in space group $Pnma$ is -6.22 eV per formula unit, also calculated with vdW-DF-CX. The zero point vibrational energy has not been taken into account when calculating the formation energies.

5.2 Electronic structure

From the electronic band structure (Figure 5.4) it is apparent that WO_2 in space group $P2_1/c$ is metallic. The orthorhombic structure on the other hand is semiconducting with a band gap of 0.57 eV. The band structure of the orthorhombic structure is shown in Figure 5.5. The nature of the band gap in orthorhombic WO_2 is different than the band gap of WO_3 (Section 6.2). In WO_3 the band gap splits oxygen-2p and tungsten-5d states similar to the situation seen in monoclinic WO_2 in the energy gap between -3 eV and -2 eV in Figure 5.6 which is well below the Fermi energy. In orthorhombic WO_2 the valence band and conduction band consists of similar states (Figure 5.7) which is a characteristic for a so called Mott insulator. The band gap is usually underestimated within standard DFT calculations, and therefore, HSE06 has been used to calculate the band gap for orthorhombic WO_2. The HSE06 calculation is performed on the structure that is obtained from relaxation with vdW-DF-CX. The band gap with HSE06 is 1.46 eV but the structure is not close to the equilibrium structure for HSE06 since forces of around 1 eV is present.

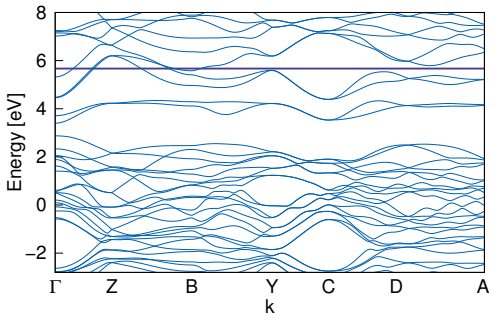

Figure 5.4: The electronic band structure for monoclinic WO_2 in space group $P2_1/c$. The Fermi energy is indicated with the line at 5.67 eV.

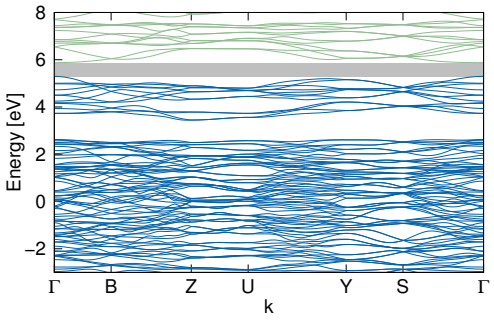

Figure 5.5: The electronic band structure for orthorhombic WO_2 in space group $Pnma$. The blue color indicate that a band is occupied while the green color indicate that the band is unoccupied at 0 K.

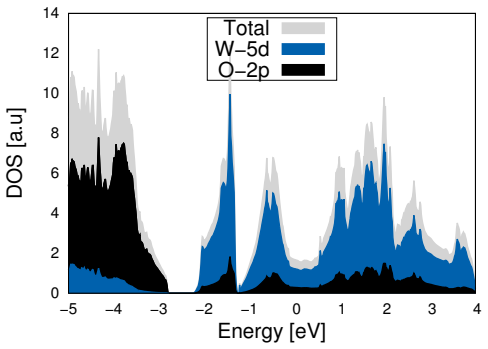

Figure 5.6: The electronic density of states for monoclinic WO_2 in space group $P2_1/c$. The Fermi energy is located at 0 eV.

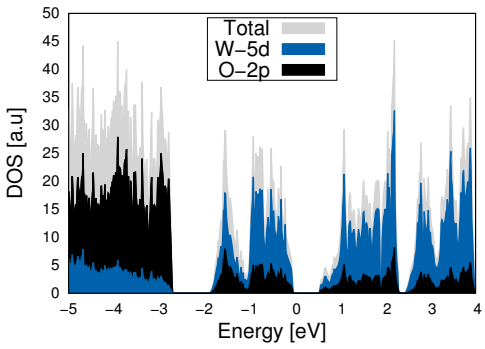

Figure 5.7: The electronic density of states for orthorhombic WO_2 in space group $Pnma$. The energy is shifted so that the Fermi energy is located at 0 eV.

5.3 Phonons

The phonon dispersion relation for monoclinic WO_2 is shown in Figure 5.8. The crystal structure is dynamically stable and the high frequency phonons are mainly due to rapid oscillations involving the oxygen atoms. Close to the zone center the acoustic phonons frequencies exhibit a linear dispersion from which the elastic response can be extracted. The phonon dispersion for orthorhombic WO_2 is shown in Figure 5.9.

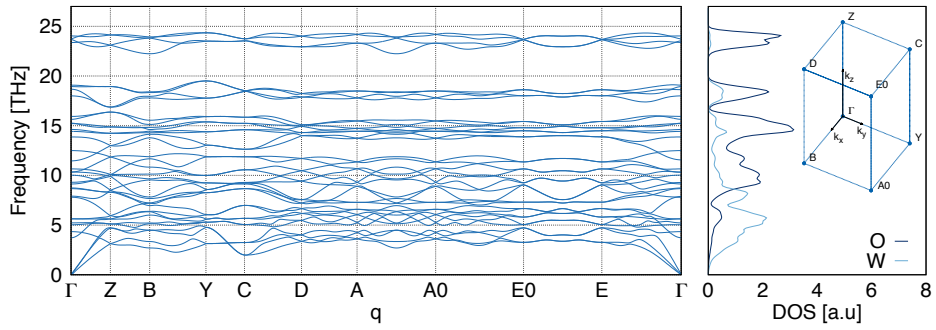

Figure 5.8: The phonon dispersion relation for monoclinic WO_2 in space group $P2_1/c$ (ITC no. 14).

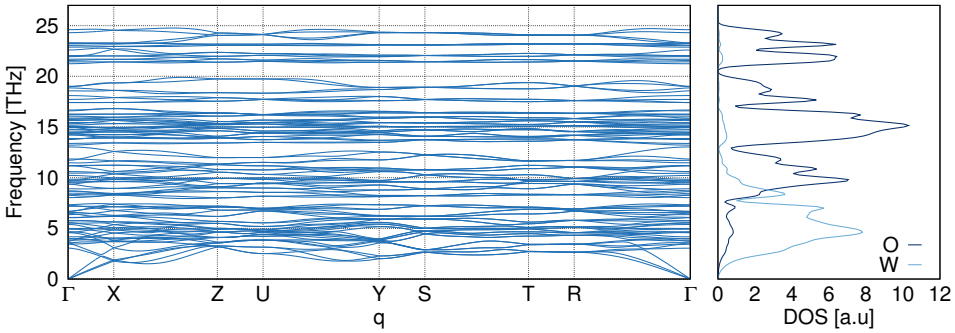

Figure 5.9: The phonon dispersion for orthorhombic WO_2 in space group $Pnma$ (ITC no. 62).

5.4 Defects

Only defects in monoclinic WO_2 in space group $P2_1/c$ were considered since it is the relevant structure from literature.

5.4.1 Vacancies

The vacancy formation energies have been calculated with a relaxation criterion of 20 meV/Å for forces acting on the ions. A plane wave cutoff energy of 600 eV has been used, slightly less than what was used for structural relaxation, the reason being that the defect energies are not as sensitive to numerical precision as the phonon calculations which was the main reason for using these very tight convergence criteria. The formation energies of the oxygen vacancies in monoclinic

WO_2 have values of 2.48 eV and 3.04 eV in the W-rich limit and 2.98 eV and 3.54 eV in the O-rich limit. The formation energy of the tungsten vacancy is low with a formation energy of 1.48 eV in the O-rich limit and 2.46 eV in the W-rich limit. The results are compiled in Table 5.5. The formation energy for the oxygen vacancies does not change much between the 12 atom unit cell and the 192 atom supercell, which indicate that the finite size effect is small in this material.

Table 5.5: Formation energy of vacancy defects in WO_2 in space group $P2_1/c$ in units of eV. The values are given for different supercell sizes and for limiting cases of the chemical potential.

	W-rich limit			O-rich limit		
	12	96	192	12	96	192
$V_O(1)$	2.49	2.53	2.48	2.99	3.03	2.98
$V_O(2)$	3.00	3.07	3.04	3.50	3.57	3.54
V_W		2.38	2.46		1.40	1.48

The values in Table 5.6 were calculated with respect to W and WO_3. The thermodynamical boundary conditions are illustrated in Figure 3.5.

5.4.2 Interstitials

Oxygen interstitial formation energies were calculated for different positions in WO_2. The structure is relatively open, which makes it probable for the lattice to host interstitial atoms. The interstitial configurations are visualized in Figures 5.10 and 5.11.

The interstitial formation energy can be found in Table 5.6. The self-interstitial where two oxygen positions sharing a lattice point in a dumbbell configuration centered at a lattice point is the energetically favorable oxygen addition to the system. Tungsten, because of the large size of the atom, has not been considered as an interstitial defect.

Table 5.6: Formation energy of oxygen interstitials in WO_2 in space group $P2_1/c$ in units of eV. The values have been computed with a supercell consisting of 96 atoms. The position refers to configurations shown in Figures 5.10-5.11

Position	W-rich limit	O-rich limit
1	4.18	3.68
2	5.74	5.24

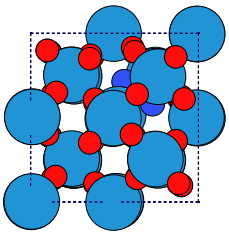

Figure 5.10: Oxygen interstitial configuration 1. The oxygen interstitial shares a lattice point with a native oxygen in a dumbbell interstitial configuration in the ⟨110⟩-direction

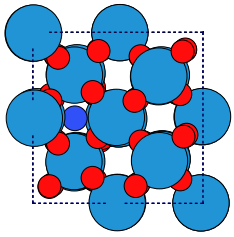

Figure 5.11: Oxygen interstitial configuration 1. The oxygen interstitial is placed in a void in the [001]-plane.

5.4.3 Oxygen migration

In WO_2 as opposed to W there are many more migration paths by which oxygen can move. To calculate the migration barrier for all of them would be very time consuming. Therefore, one path (Figure 5.12) in the ⟨100⟩-direction has been selected to obtain some knowledge of oxygen transport in WO_2. The path was selected based on static calculations with 3 images. The initial configuration is a vacancy in site 2 ($V_O(2)$) and the final state is a vacancy in site 1 ($V_O(1)$). The climbing nudge elastic band has been utilized and the calculation has been limited to 5 images, due to the high computational cost. The migration barrier amounts to 2.41 eV, which is shown in Figure 5.13, which makes oxygen diffusion mediated by vacancies not a common event, even at very high temperatures such as those found at the wall in fusion reactors.

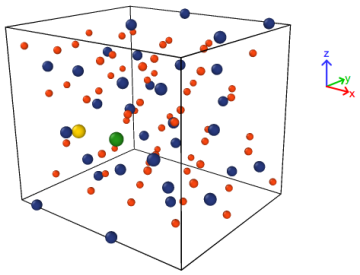

Figure 5.12: Initial and final configuration in [001]-plane as indicated by yellow respective green colors.

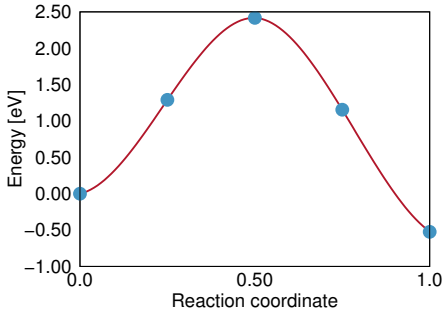

Figure 5.13: Migration barrier for oxygen vacancy migration in $\langle 100 \rangle$ from $V_O(2)$ to $V_O(1)$.

6 Tungsten trioxide

In this section the structural properties and electronic band structure are reported for all polymorphs of WO_3. Results of the lattice dynamics calculations are then reported, and an explanation of the origin of the imaginary phonon found in the monoclinic ground state structure is offered.

Following the phonon part, the defect calculations are reported where formation energies for oxygen and tungsten defects have been calculated. Finally, the result for the Y substitutional defect is reported.

6.1 Structure

The departing point for the structural calculations was experimentally determined crystal structures, where references to experiments can be found in Table 1.1. Because of the large atomic difference between oxygen and tungsten, it is difficult to resolve the oxygen positions with x-ray experiments, therefore, neutron experiments have been used to as far extent as possible. The number of atoms in the unit cell for the different phases of WO_3 varies between 8 for the tetragonal phase and 32 for the orthorhombic and triclinic phases. Also, the unit cell of the monoclinic structure in space group $P2_1/n$ contains 32 atoms. The large unit cells are largely due to the tilting of the oxygen octahedra, since tilting one octahedron automatically makes the neighboring octahedron tilt in the opposite direction, thus requiring a doubling of the unit cell.

Furthermore, the calculations on the ideal cubic cell has been included because it allows for comparison with other theoretical studies, but also because it carries some relevance as some studies indicate that it can be stabilized by doping.

The ability to describe the structure theoretically is largely dependent on the type of exchange correlation functional used, but locating the minimum is in almost all cases a lengthy process which usually required around 300 ionic displacements to come to a fully relaxed geometry with interatomic forces less than 5 meV/Å. This is probably due to the very flat potential energy landscape close to the equilibrium structure and to this end, several functionals cannot properly describe the triclinic and orthorhombic phases, as can be seen in Table 6.1.

For all structural calculations a plane wave cutoff energy of 700 eV and a Monkhorst-Pack $k-$point grid with a spacing of 0.2 $Å^{-1}$ was used, corresponding in most cases to a $5 \times 5 \times 5$ grid, furthermore, Gaussian smearing with a smearing parameter of 0.2 eV was used. The convergence with respect to the smearing was

checked and the result does not change for a smearing parameter of 0.1 eV. The reason that such a large basis set and dense integration mesh has been used in the structural calculations is related to the phonon calculations, which require very high precision in the force calculations.

The error in describing the lattice parameters for all phases and functionals is shown in Figures A.1 to A.6 in Appendix A and in Table 6.4 the structural parameters for have been compiled for calculations with vdW-DF-CX.

From a comparison of the different functionals it is clear that PBE in all cases overestimates the lattice constants by the largest amount, with AM05 in second place. The difference between AM05 and PBEsol, however, in terms of lattice constants is small in all cases, peaking in the monoclinic phase where AM05 has a maximum error of 0.16 Å and PBEsol 0.11 Å for the lattice parameter b. In some phases, such as one tetragonal phase vdW-DF-CX and PBE estimates the lattice parameter in qualitatively different ways: while vdW-DF-CX (and PBEsol) underestimates the two equivalent lattice constants PBE overestimates it. The description of the low temperature phases, specially the monoclinic in space group Pc is the most important in this work. In this regard vdW-DF-CX outperforms the other in terms of matching experimental and computed lattice parameters.

The monoclinic phases (Pc and $P2_1/c$) have almost identical energies and are only differentiated by symmetry. There is a relatively large energy difference between the orthorhombic structures. This is true in the tetragonal structure as well.

The functionals that accurately predicts that the monoclinic phase in space group Pc is the ground state are vdW-DF-CX and PBEsol. PBE predicts the orthorhombic phases to be the most stable, while PBEsol has the monoclinic as the lowest energy phase with the orthorhombic phases just 0.001 eV above. AM05 has the tetragonal phase as the ground state, which is quite surprising, since it is the high temperature phase. AM05 also has problems converging the calculations for oxygen and oxygen dimer which makes it not as useful as the other functionals for future calculations when considering formation energies.

The hexagonal phase of WO_3 has a higher formation energy than the monoclinic room temperature phases ($P2_1/n$ and $P2_1/c$), which makes this a metastable phase unless entropic effects for the hexagonal phase are much higher than for the monoclinic phase.

The computational formation energy is -8.775 eV for monoclinic WO_3 in space group Pc with vdW-DF-CX, which is in very good agreement with the experimental value of -8.736 eV (deviates 0.5%). The formation energy calculated with PBE is around 3% off and the PBEsol value is off by around 6%. The experimental formation energy is also at standard state at room temperature which means that in theory the computed and experimental values should deviate.

Table 6.1: Cohesive energies in units of meV/f.u. for all WO_3 structures calculated with different exchange correlation functionals. The value of the cohesive energy is given for the experimental ground state structure Pc (ITC no. 7). For the other structures only the difference relative to the Pc structure is given. For the calculations with AM05, only relative cohesive energies exists.

Space group	ITC no.	vdW-DF-CX	PBE	PBEsol	AM05
Triclinic					
$P\bar{1}$	2	2.7			
Monoclinic					
Pc	7	−30722.1	−27125.8	−28598.7	
$P2_1/c$	14	0.2	0.3	0.6	1.4
$P2_1/n$	14	3.1			
Orthorhombic					
$Pcnb$	60	9.2	−4.4		
$Pnma$	62	38.8	−5.6	0.8	30.0
Tetragonal					
$P\bar{4}2_1m$	113	39.6	−4.0	1.2	−4.0
$P4/nmm$	129	58.4	14.8	17.2	−13.0
$P4/ncc$	130	26.0	12.8	8.4	
Hexagonal					
$P6/mmm$	191	175.2	126.8	88.3	
$P6_3/mcm$	193	4517.2	4508.4	4605.3	

In monoclinic WO_3 in space group $P2_1/c$ (ITC no. 14), there is one unique tungsten position and the tungsten oxygen bond lengths are compiled in Table 6.2. The bond length are not the same in any direction and the largest difference is seen in the $\langle 001 \rangle$ direction where there are alternating W-O bonds with length 2.15 Å and 1.78 Å. In monoclinic WO_3 in space group Pc there are 6 unique oxygen positions and 2 unique tungsten positions, however, because of the similarity of the phases Pc and $P2_1/c$, the unique oxygen and tungsten positions in Pc should be paired in a similar way as in $P2_1/c$.

Table 6.2: Bond lengths in units of Å for the monoclinic WO_3 in space group $P2_1/c$ (ITC no. 14) and tetragonal WO_3 in space group $P4/ncc$ (ITC no. 130).

Direction	$P2_1/c$	$P4/ncc$
$\langle 1\bar{1}0 \rangle$	1.84	1.91
$\langle \bar{1}\bar{1}0 \rangle$	1.85	1.91
$\langle 110 \rangle$	2.00	1.91
$\langle \bar{1}10 \rangle$	1.99	1.91
$\langle 001 \rangle$	2.15	2.17
$\langle 00\bar{1} \rangle$	1.78	1.77

An investigation of how the hybrid functional HSE06 describes the structure of WO_3 in space group Pc was undertaken. A force calculation on the ions with HSE06 on the vdW-DF-CX structure reveals very large forces, on the order of 1 eV/Å, making it difficult to use HSE06 to align the band gap. A relaxation in which only 30 ionic steps were allowed during relaxation from the equilibrium vdW-DF-CX structure was performed. The k-point mesh was also reduced to a $2 \times 2 \times 2$ Monkhorst-Pack grid. The result of this relaxation is shown in Table 6.3. The structure obtained by HSE06 is not an equilibrium structure, but the tilting angle defined in Figure 6.1 is close to experimental values. It is noted that neither PBE, AM05 nor PBSEsol accurately describes the tilting angle.

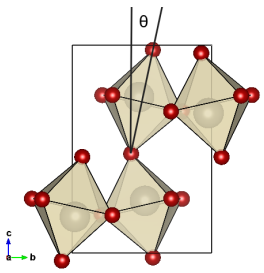

Figure 6.1: The tilting angle in b-direction defined for the experimental crystal structure of WO_3 in space group Pc (ITC no. 7).

Table 6.3: Tilting angle in b-direction in WO_3 in space group Pc (ITC no. 7) as defined in Figure 6.1.

	Tilting angle [°]
Exp.	11.86
vdW-DF-CX	12.77
PBE	5.14
AM05	4.74
PBEsol	7.29
HSE06	11.78

Table 6.4: Structural parameters for different phases of WO_3 as calculated with vdW-DF-CX and comparison with experimental data.

Space group	a[Å]	b[Å]	c[Å]	V[Å^3]	α [°]	β [°]	γ [°]
$Pm\bar{3}m$	3.806	3.806	3.806	55.14	90	90	90
Pc	5.290	5.140	7.639	207.51	90	92.39	90
Exp. [11]	5.277	5.155	7.663	208.4	90	91.76	90
$P\bar{1}$	7.353	7.412	7.627	415.51	88.49	88.22	88.45
Exp. [12]	7.313	7.525	7.689	422.9	88.85	90.91	90.94
$P2_1/c$	5.288	5.132	7.635	207.01	90	92.39	90
Exp. [14]	5.261	5.128	7.650	206.3	90	92.05	90
$P2_1/n$	7.416	7.401	7.577	415.75	90	91.61	90
Exp. [13]	7.297	7.539	7.688	422.9	90	90.91	90
$Pcnb$	7.361	7.492	7.688	423.96	90	90	90
Exp. [15]	7.333	7.573	7.740	429.9	90	90	90
$Pnma$	7.514	7.685	7.792	449.96	90	90	90
Exp. [16]	7.341	7.770	7.754	430.9	90	90	90
$P\bar{4}2_1m$	7.606	7.606	3.887	224.88	90	90	90
Exp. [17]	7.39	7.39	3.88	211.9	90	90	90
$P4/nmm$	5.342	5.342	3.937	112.33	90	90	90
Exp. [18]	5.272	5.272	3.920	109.0	90	90	90
$P4/ncc$	5.225	5.225	7.878	215.05	90	90	90
Exp. [15]	5.276	5.276	7.846	218.4	90	90	90
$P6/mmm$	7.419	7.419	3.816	181.91	90	90	120
Exp. [19]	7.298	7.298	3.899	179.8	90	90	120
$P6_3/mcm$	7.578	7.578	9.123	453.70	90	90	120
Exp. [20]	7.324	7.324	7.553	356.0	90	90	120

From here on the monoclinic and triclinic phases will be referred to as low-temperature phases while the other are referred to as high-temperature phases.

6.2 Electronic structure

WO_3 falls in the category of wide gap semiconductors when considering the experimental band gap of 2.75 eV [46] for the monoclinic structure. The computed band

structures for the monoclinic phases are shown in Figures 6.2-6.4. The Brillouin zone path for both monoclinic phases is found in Figure 6.6.

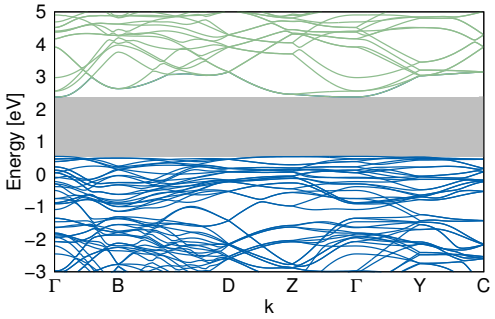

Figure 6.2: Band structure for monoclinic WO_3 in space group Pc (ITC no. 7)

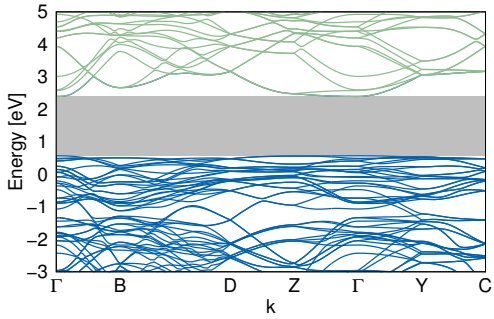

Figure 6.3: Band structure for monoclinic WO_3 in space group $P2_1/c$ (ITC no. 14).

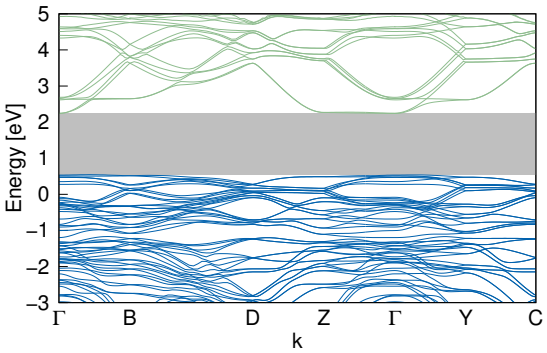

Figure 6.4: Band structure for monoclinic WO_3 in space group $P2_1/n$ (ITC no. 14)

The band structures of the two monoclinic phases in space group Pc respectively $P2_1/c$ are very similar, further suggesting that there is no practical difference between the two phases. The valence band is very flat in both phases making a distinction of the type of band gap not feasible. The band gap, but also the location of the valence band maximum is important for defect concentrations since those quantities are related to the electron chemical potential. The differences in the band structure between Pc and $P2_1/n$ are much more distinct than between Pc and $P2_1/c$. The $P2_1/n$ structure exhibits more dispersion in the valence band, but the qualitative features of the conduction band around Γ are similar.

The results for the band gap is shown in Table 6.5. The vdW-DF-CX functional clearly underestimates the band gap. This is a common problem with local and

semi-local DFT exchange-correlation functionals. Hartree-Fock methods on the other hand often overestimates the band gap and the hybrid functional which has some of the Hartree-Fock exchange overestimates the band gap by around 8%. It should be noted that for HSE06, the vdW-DF-CX equilibrium structure has been used for band structure calculations, however, the vdW-DF-CX structure is not close to the HSE06 equilibrium since forces of slightly less than 1 eV/Å appear. In Figure 6.5 the partial density of states is shown. It is clear that the valence band consists mainly of oxygen $2p$ states while the conduction band consists of tungsten $5d$ states. This is in line with mostly ionic bonds and a charge transfer type semiconductor.

Table 6.5: Band gap for different functionals for monoclinic WO_3 in space group Pc (ITC no. 7). The HSE06 calculation was performed on the vdW-DF-CX equilibrium structure.

	E_{VBM} [eV]	E_{CBM} [eV]	E_g [eV]	Error
HSE06	−0.43	2.52	2.95	+8%
vdW-DF-CX	0.57	2.40	1.83	−33 %
PBE	0.28	1.96	1.68	−39 %
Exp [46]			2.75	

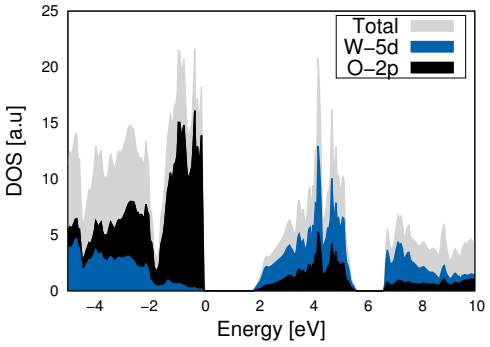

Figure 6.5: Partial density of states for monoclinic WO_3 in space group Pc (ITC no. 7).

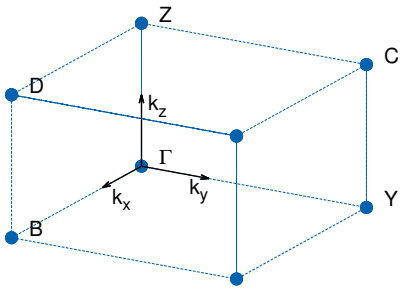

Figure 6.6: Schematic Brillouin zone for the monoclinic phases.

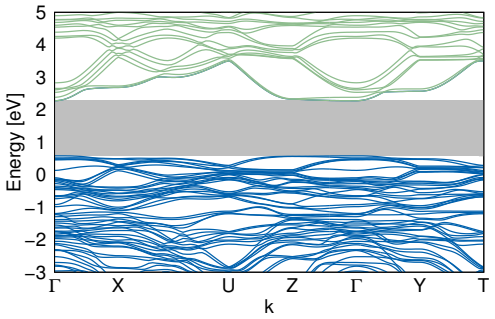

Figure 6.7: Band structure for triclinic WO_3 in space group $P\bar{1}$ (ITC no. 2).

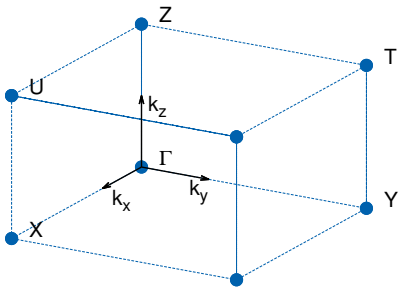

Figure 6.8: Schematic Brillouin zone for triclinic and orthorhombic structures.

The band structure of the triclinic phase is shown in Figure 6.7 for the Brillouin zone path in Figure 6.8. The valence band is flat but has more curvature than in the monoclinic structures. The conduction band has similarities with the monoclinic structures, in particular along the direction from Γ to X and the corresponding Γ-B line, which exhibits strong dispersion. In the Γ-Z direction in both triclinic and monoclinic structures there is a very flat conduction band and a very flat valence band.

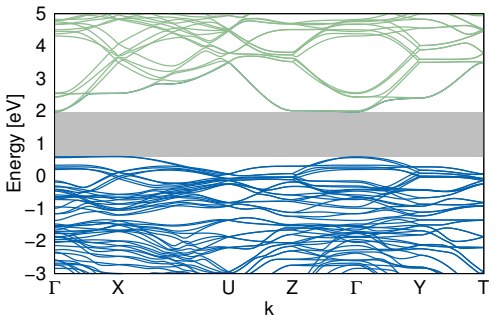

Figure 6.9: Band structure for orthorhombic WO_3 in space group $Pcnb$ (ITC no. 60).

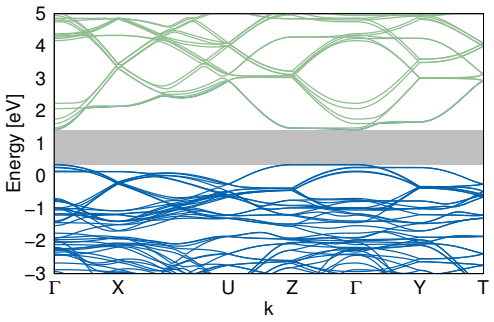

Figure 6.10: Band structure for orthorhombic WO_3 in space group $Pnma$ (ITC no. 62).

Figures 6.9 and 6.10 show the band structure for the orthorhombic phases. The conduction band for both orthorhombic structures is very similar and shares all distinct features. There is also not a big difference between the orthorhombic and triclinic conduction bands. This not surprising since the conduction band is mainly composed of tungsten 5d states and the tungsten atoms are located in similar environments in both structures. The main difference is the tilting of

octahedra, which has the effect that the $2p$ states of oxygen, which makes up the valence band is different. This is evident from the very flat behavior between Γ and Z in the space group *Pnma* while this feature is not there for space group *Pcnb* structure. The most pronounced difference between the two orthorhombic phases is the tilting of octahedra which is not present in space group *Pnma* to the same extent as in *Pcnb*, which has a similar degree of tilting as the triclinic phase.

There are some similarities between the orthorhombic and tetragonal structures (Figure 6.11-6.13). For the orthorhombic and tetragonal structures there are two proposed configurations of the oxygen octahedral network, where in one configuration the octahedra are not tilted. This difference is resulting in relatively different results of the electronic structure where the non-tilted structure has a significantly more narrow band gap than the tilted configuration. Furthermore, this non tilted configuration adds more curvature to the valence band than the tilted. It is noted that it is mainly the valence band that is affected by the octahedral tilting. In Table 6.6 the band gap energies and type of band gap is summarized for all phases of WO_3. The largest band gaps belongs to the low temperature structures. The hexagonal phases Figure 6.15-6.16 have the smallest band gaps.

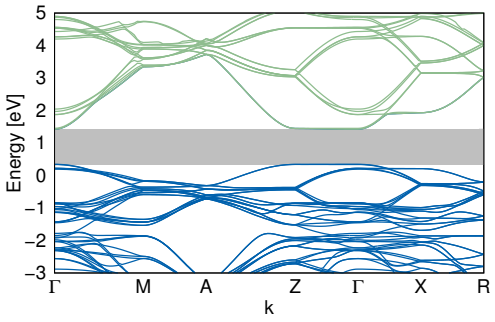

Figure 6.11: Band structure for tetragonal WO_3 in space group $P\bar{4}2_1m$ (ITC no. 113).

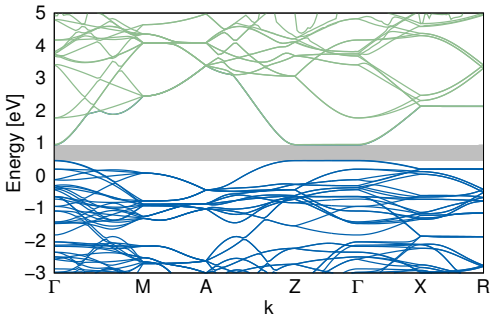

Figure 6.12: Band structure for tetragonal WO_3 in space group $P4/nmm$ (ITC no. 129).

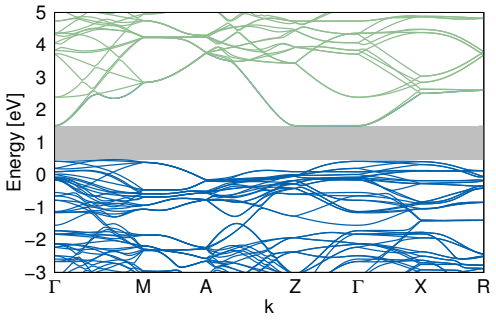

Figure 6.13: Band structure for tetragonal WO_3 in space group $P4/ncc$ (ITC no. 130).

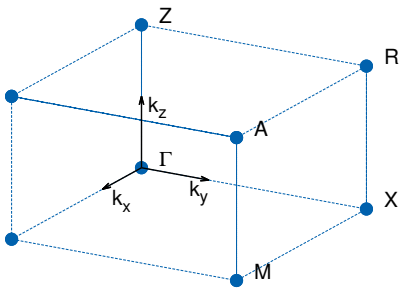

Figure 6.14: Brillouin zone for tetragonal structures.

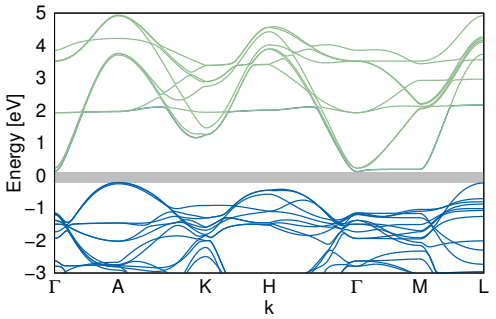

Figure 6.15: Band structure for hexagonal WO_3 in space group $P6/mmm$ (ITC no. 191).

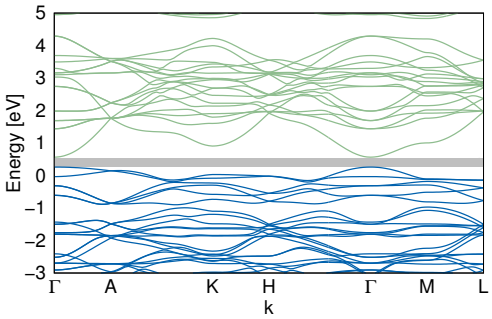

Figure 6.16: Band structure for hexagonal WO_3 in space group $P6_3/mcm$ (ITC no. 193).

Table 6.6: Band gap energies for different phases of WO_3 as calculated with vdW-DF-CX. The column labelled ΔE contains the relative cohesive energies with respect to monoclinic WO_3 in space group Pc (ITC no. 7).

Space group	ITC no.	Band gap [eV]	Type	ΔE [meV/f.u.]
Pc	7	1.83	d	0
$P2_1/c$	14	1.83	i	0.2
$P\bar{1}$	2	1.76	d	2.7
$P2_1/n$	14	1.70	i	3.1
$Pcnb$	60	1.37	i	9.2
$P4/ncc$	130	1.05	i	26.0
$Pnma$	62	0.91	d	38.8
$P\bar{4}2_1m$	113	0.84	d	39.6
$P4/nmm$	129	0.48	i	58.4
$P6/mmm$	191	0.34	i	175.2
$P6_3/mcm$	193	0.30	d	4517.2

6.3 Phonon structure

The lattice dynamics of WO_3 have not been thoroughly studied with a computational approach earlier, and only limited experimental data for the phonons exists. In this section, the phonon calculations are presented for all phases of WO_3 and related to other studies and experiments if possible.

6.3.1 Low temperature phases

The lattice dynamics of WO_3 are complex. It is a polar insulator and as such it is expected to experience long range Coulomb interactions, which makes studies based on finite displacements and supercells difficult. The monoclinic and triclinic phases have real Γ-point frequencies, which means that the unit cell is stable. The full BZ phonon dispersion was calculated for two phases (Pc and $P2_1/c$) of monoclinic WO_3, revealing very similar vibrational structures. In Figure 6.17 and 6.18, the phonon dispersion and partial density of states is shown for Pc and $P2_1/c$. The most striking feature of the monoclinic phases is the imaginary mode between Γ and Z. The imaginary mode may be a consequence of bond length variation and the small restoring forces associated with octahedral tilting. This mode is studied in detail in the next section.

The triclinic phase has a large unit cell and low symmetry. Experimental studies [47] suggests that this phase is often found coexisting with monoclinic phases at low temperatures making it necessary to establish wether this material is stable or not.

The full Brillouin zone dispersion relation shows optical instabilities (Figure 6.19) at the Γ-point and a similar acoustic instability as the one that is present in the monoclinic structures. Because of the combination of large system and low symmetry in triclinic phase, the high precision in the phonon calculations could not be maintained. The plane wave cutoff energy used was 530 eV and the k-spacing was set to of 0.3 Å^{-1}. The optical instability may be due to low precision in the calculations. The monoclinic $P2_1/n$ has real Γ-point frequencies but exhibits similar acoustic instabilities as the other monoclinic phases. The full phonon dispersion for the monoclinic $P2_1/n$ structure was not calculated.

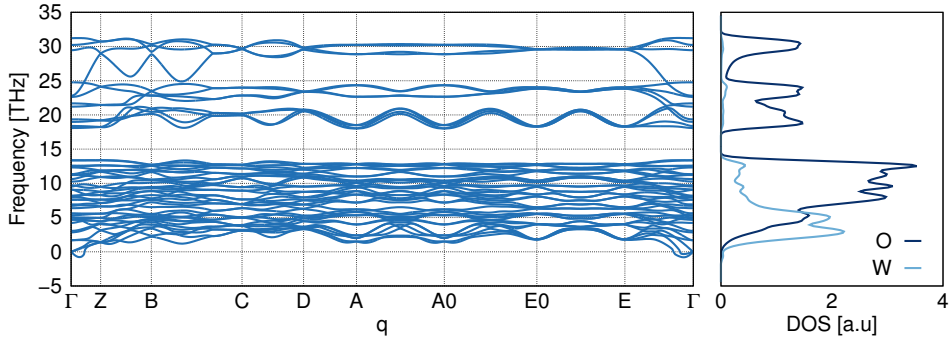

Figure 6.17: The phonon dispersion relation and density of states for monoclinic WO_3 in space group Pc as calculated with vdW-DF-CX. The Brillouin zone path is shown in Figure 6.18.

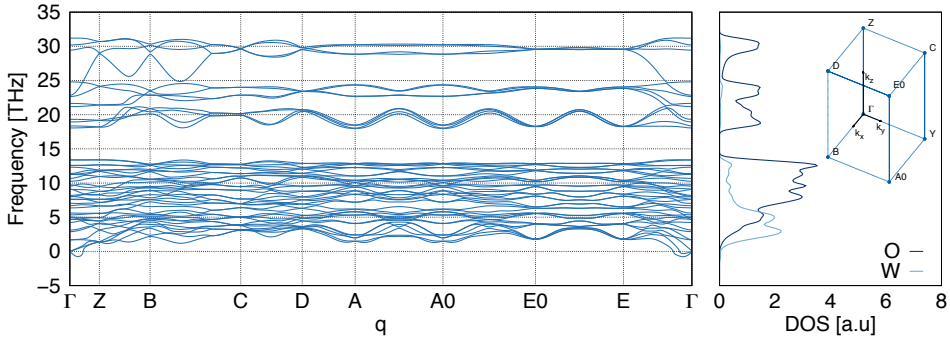

Figure 6.18: The phonon dispersion relation and density of states for monoclinic WO_3 in space group $P2_1/c$ as calculated with vdW-DF-CX. The high symmetry points A and E are not shown in the schematic Brillouin zone as the points are related to A0 and E0 by a change of sign of the k_y-component.

The orthorhombic phases has imaginary zone center modes. It is therefore not sensible to calculate the full Brillouin zone dispersion for the orthorhombic phases

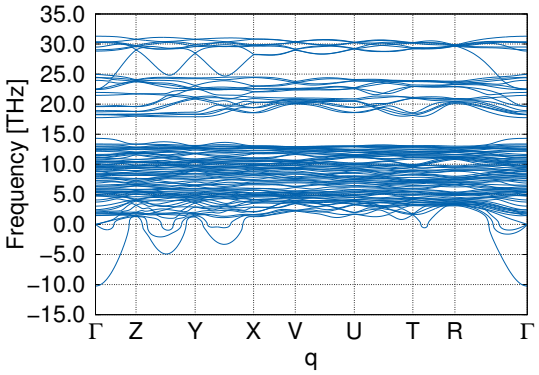

Figure 6.19: The phonon dispersion relation for the triclinic phase in space group $P\bar{1}$ (ITC no. 2). The structure has imaginary Γ-point frequencies.

also because of the large unit cell and very low symmetry. It is possible to follow the imaginary zone center mode by displacing the structure along the phonon normal coordinates. The resulting crystal structure exhibits monoclinic symmetry and belongs to space group $P2_1/n$. This transition, by a zone center mode is described in experiments [48]. This kind of structural relationship between different crystal structures is found only in this case in the phonon calculations. This fact does not rule out other structural relations described by linear combinations of different displacements patterns.

All low temperature phases (monoclinic, triclinic and orthorhombic) have very similar density of states, as shown in Figure 6.20.

In the low temperature phases there is a distinct peak at around 30 THz, which corresponds to rapid oxygen oscillations just as in tungsten dioxide in Figure 5.8.

In Figure 6.21 the high temperature and hexagonal structure vibrational DOS are shown. The hexagonal phases has large imaginary peaks that are not found in other phases, which underpins the structural difference compared to the other phases.

6.3.1.1 The imaginary acoustic mode in monoclinic WO_3

In spite of WO_3 in space group Pc being the ground state the phonon dispersion described above (Figure 6.17) exhibits imaginary acoustic modes near the zone center. Because of the structural similarity between the two monoclinic phases, the imaginary mode in WO_3 in space group $P2_1/c$ is studied since symmetry reduces the computational cost by almost half for space group $P2_1/c$ compared to Pc. In order to investigate wether the mode results from numerical noise, or is an actual instability, the computational parameters related to electronic and phonon structure calculations were varied in order to exclude that the instability is of due

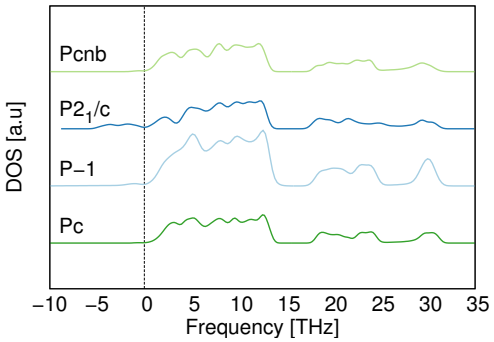

Figure 6.20: Phonon DOS for the monoclinic, triclinic and orthorhombic space groups.

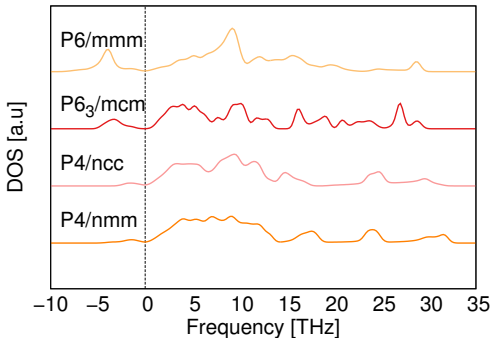

Figure 6.21: Phonon DOS for the tetragonal and hexagonal space groups.

numerical inaccuracies. The result of the parameter study is found in Appendix B for the ideal cubic phase. The numerical noise associated with these parameters is generally small. Some effect could be seen when increasing the displacement but the overall effect was too low to lift the imaginary mode. The supercell method to calculate phonons is an approximation in itself, therefore, the size effect in the unstable direction was investigated.

In fact Figure 6.22 shows that the dynamical matrix has not converged with respect to system size with respect to the transverse acoustic modes near Γ. From Figure 6.22 it can be inferred systems that are larger in the $\langle 001 \rangle-$direction have a larger range of stability. The $1 \times 1 \times 2$ supercell can sustain acoustic phonons with half the wavelength of the Brillouin zone, while the $1 \times 1 \times 9$ supercell is stable for acoustic phonons of still longer wavelengths. This reduction of amplitude of the imaginary mode seems to have levelled off at $1 \times 1 \times 9$, however, periodic boundary conditions in the other spatial dimensions may still have an influence.

Imaginary phonons are associated with lower energy structures. Therefore, supercells that supposedly can support the imaginary modes were constructed and displaced along the normal mode. The mode under investigation is the imaginary mode in the $1 \times 1 \times 2$ supercell in Figure 6.22, and the structure is displaced along the normal mode corresponding to a $q-$point of $(0, 0, 0.125)$ with a supercell of dimension $1 \times 1 \times 8$, the result is seen in Figure 6.23. The imaginary phonon mode is not captured, but rather it seems like the imaginary mode is 'running' in front of the displacement. Interpolating the results in Figure 6.22, the $1 \times 1 \times 8$ supercell does not exhibit imaginary phonons at the exact q-points.

This makes it difficult to resolve the question whether this mode is associated with a structural or numerical instability by means of mode following. The $q-$points, where the dynamical matrix is exact with respect to system size are

all real for all system sizes, which indicate that the instability is related to the finite size of the crystal structure that the phonon calculations are performed on. Analyzing the force constants, defined in equation (3.3), the magnitude of the force

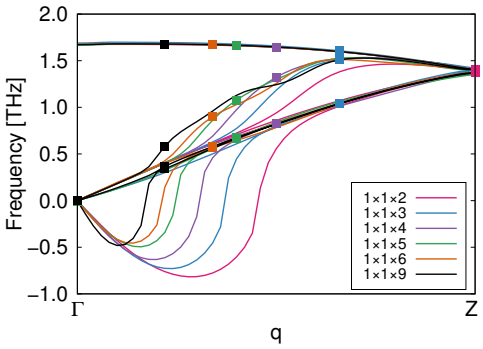

Figure 6.22: Imaginary mode in monoclinic WO_3. The solid markers indicate the smallest exact $q-$points that can be supported by the supercell.

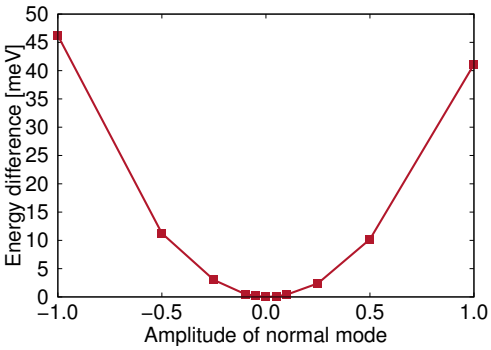

Figure 6.23: Energies for structures along the imaginary phonon mode at (0,0,0.125) q-point. The maximum amplitude of 1.0 corresponds to displacements of 0.035 Å for the oxygen atoms and 0.030 Å for the tungsten atoms.

constants are not decaying rapidly in WO_3 as there are large values at a atomic separation distance of 4 Å, which are shown in Figure 6.24, which may influence the result. Comparing with the results for WO_2 (space group $P2_1/c$) in Figure 6.25, the force constants decay quickly and the dispersion has real frequencies at all $q-$points.

The long range behavior of the force constants may be related to high effective charges of the atoms and the lack of screening, this behavior may also be enhanced by the mechanical properties of the octahedra. Figure 6.24 indicate rather high force constants at long distances such as at around 7.7 Å, which corresponds to the interaction between a tungsten atom and an oxygen atom on the opposite side of the neighboring octahedron. The force constants in metallic materials with efficient screening decay as r^{-5}, while force constants in polar insulators decay as r^{-3}, similar to the situation in Figure 6.25 and 6.24.

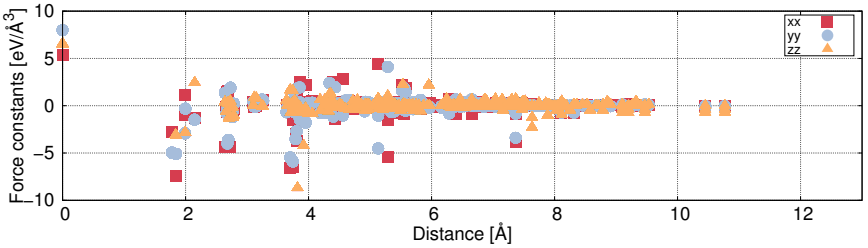

Figure 6.24: Force constants of monoclinic WO_3 in space group $P2_1/c$ (ITC no. 14) as a function of atomic separation for $2 \times 2 \times 2$ super cell calculated with vdW-DF-CX.

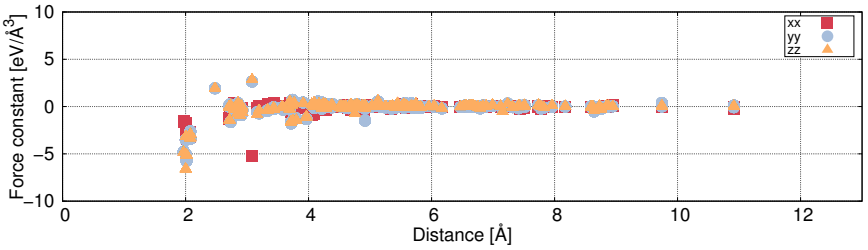

Figure 6.25: Force constants for WO_2 in space group $P2_1/c$ as a comparison. The force constants has been calculated with vdW-DF-CX and a $2 \times 2 \times 2$ supercell.

The hard potential setup for W, where 14 valence electrons for tungsten are used in calculations, was also used for phonon calculations, the imaginary mode was still there, and the frequencies for the $1 \times 1 \times 2$ supercell was similar to the 6 valence electron potential calculations. Attempts to stabilize WO_3 with smaller lattice parameters were undertaken as well, and the acoustic phonon can in fact be stabilized at long wavelengths at the cost of additional imaginary optical frequencies and an acoustic instability at shorter wavelengths.

The explanation offered at this moment is that the structure is so soft and that long range interaction affect the force constants so that at points where the dynamical matrix is not exact, the image interaction is too large which causes a numerical instability.

Doping in WO_3

In connection with the imaginary mode, long range interactions should be screened by adding electrons to the system. n-doping the monoclinic structure results in a more stable structure and the imaginary phonon along the Γ-Z direction is immediately stabilized with a charge doping of 0.5 electrons per unit cell. This can be understood to be an effect of electronic screening together with the long ranged

force constants. In the pure material, without doping, the tungsten atoms move with a very high positive charge (the Born effective charge has maximum value of 10) which permits very long ranged Coulomb interaction in the material.

The screening of electrons may make the force constants decay more rapidly and the situation is more like a metallic system where the force constants decay as r^{-5} because of the efficient screening. If the only stabilizing mechanism is due to screening, the material could be dynamically stable, and calculations on a larger system would show that. Unfortunately, going to a $3 \times 3 \times 3$ supercell increases the number of atoms from 128 to 432. While it is possible, at this moment accurate phonon calculations on a system of that size is too expensive.

As will be presented in the section on defects, a neutral oxygen vacancy may cause unintentional n-type conductivity and a neutral oxygen vacancy can therefore be thought of as dopant. This dopant, however, causes no direct change in the phonon dispersion except the introduction of another imaginary mode, which in some way contradicts the result from the n-type doping if it is merely a numerical instability due to long ranged force constants that is seen. The most convincing argument is that the instability in the $\langle 010 \rangle$ is not stabilized with n-type doping, however, that mode is stabilized with p-type doping.

Studying the effect of defects, limitations on system size has to be enforced because of the symmetry reduction a defect introduces, and hence, the computational cost increases significantly. To this end, studies on the $1 \times 1 \times 2$ supercell consisting of 31 atoms has been conducted for the neutral vacancy defect. This defect is placed in the WO_2-plane.

The phonon dispersion in $\langle 001 \rangle$ is very flat and an imaginary optical mode appears as well as a qualitative different behavior of the acoustic mode which does not turn up again, instead monotonically decreasing until it reaches the Brillouin zone boundary. In this case the optical phonon mode may represent a structure with lower symmetry so the crystal was displaced along this normal mode and fully relaxed to the same criterion as the usual unit cell and the imaginary mode appeared in a similar manner.

6.3.2 High temperature phases

All high temperature phases, including the ideal cubic phase, has imaginary Γ-point optical phonons which means the unit cell is unstable against optical long wavelength displacements. In Figure 6.21 the DOS for the tetragonal structure is seen where it is clear that the contribution from imaginary modes is larger than in the low temperature structures. This is to be expected since these modes should be stabilized by temperature effects. Following an instability results in lower energy structures as can be seen in Figure 6.26 where the tetragonal structure has been displaced along the imaginary mode. By following this mode it seems like the

imaginary mode at the zone center is related to a phase transition to monoclinic Pc structure. There is no mentioning of a tetragonal to monoclinic transition without passing through the orthorhombic and triclinic phases.

The acoustic phonons for the high temperature phases are real close to the zone center as opposed to the low temperature phases which were unstable against some long wavelength displacements. The phonons of the high temperature phases is stabilized by temperature effects and is outside the realm of DFT, which serves as motivation for model potential fitting.

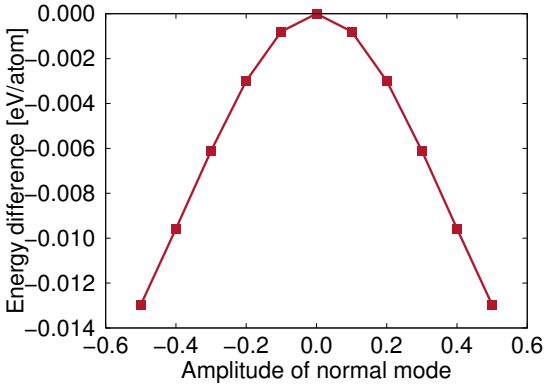

Figure 6.26: The displacement along lowest imaginary modes in tetragonal WO_3 in space group $P4/nmm$ (ITC no. 129) at Γ gives lower energy structures.

6.4 Defects

In this section, the formation energies of charged tungsten and oxygen vacancies as well as oxygen interstitials are presented. The defect formation energies has been calculated for WO_3 in space group $P2_1/c$ but because of the similarities in structure, phonons and electronic band structure between Pc and $P2_1/c$, the defect formation energies are not anticipated to change dramatically between the structures. For the defect calculations a planewave cutoff energy of 500 eV and k-spacing of 0.3 Å^{-1}.

6.4.1 Oxygen vacancy

In WO_3 in space group $P2_1/c$ there are three distinct oxygen sites. The oxygen atoms are located on Wyckoff 4e sites, which are shown in Figure 6.27. Two of the unique oxygen sites (4e(1) and 4e(3)) are located in the WO_2-plane and one is located in the O-plane (4e(2)).

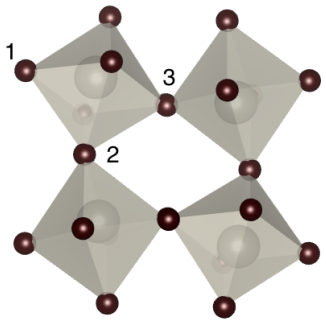

Figure 6.27: The oxygen atoms are located on Wyckoff sites 4e(1), 4e(2) and 4e(3) as indicated in the figure.

The formation energy has been calculated for different sizes of the supercell. The formation energy for an oxygen vacancy in Wyckoff site 4e(1) and 4e(3) are similar, therefore, only the supercell scaling results for oxygen vacancies in Wyckoff 4e(1) and 4e(2) are presented. The result of the finite size scaling is shown in Figure 6.28 for 4e(1) and in Figure 6.29 for 4e(2). The formation energy for an oxygen vacancy in the 4e(1) Wyckoff site has leveled off at a supercell size of 192 atoms while the formation energy of an oxygen vacancy in Wyckoff site 4e(2) has leveled of already at a 96 atom supercell since the formation energy difference between the 96 and the 192 atom supercell is small, especially for the +1 charge state and the neutral vacancy. The formation energy values are compiled in Table 6.7. It is anticipated that the $P2_1/c$ gives similar formation energies as Pc. The defect formation of a neutral defect in Wyckoff site 4e(2) was calculated to 0.67 eV for a 192 atom supercell for WO_3 in space group Pc, which does not differ from the defect formation energy calculated in space group $P2_1/c$.

Table 6.7: Formation energy of an oxygen vacancy in WO_3 in space group $P2_1/c$ in units of eV for a supercell consisting of 320 atoms for 4e(1) and 4e(3) and 192 atoms for 4e(2).

	O-rich limit			W-rich limit		
	$q=0$	$q=+1$	$q=+2$	$q=0$	$q=+1$	$q=+2$
4e(1)	3.44	1.68	−0.02	0.77	−0.99	−2.65
4e(2)	3.34	1.48	−0.22	0.67	−1.19	−2.85
4e(3)	3.44	1.68	−0.02	0.77	−0.99	−2.65

The formation energies for the charged defects depend on the chemical potential of the electrons (equation 3.6) and in Figure 6.30 the formation energy between the valence band maximum and the conduction band minimum as a function of the

chemical potential of electrons is shown. There is one charge transition level for the oxygen vacancy located on Wyckoff site 4e(2). The $+2/+1$ transition occurs at around 0.15 eV below the CBM and the oxygen vacancy is stable between the transition level and the CBM. For defects located on Wyckoff site 4e(1) and 4e(3) there are two charge transition levels, the $+2/+1$ charge transition takes place at 0.17 eV below the CBM and the $+1/0$ is located 0.09 eV below the CBM. This suggests that an oxygen vacancy acts as a shallow donor in WO_3, which would contribute to n-type conductivity.

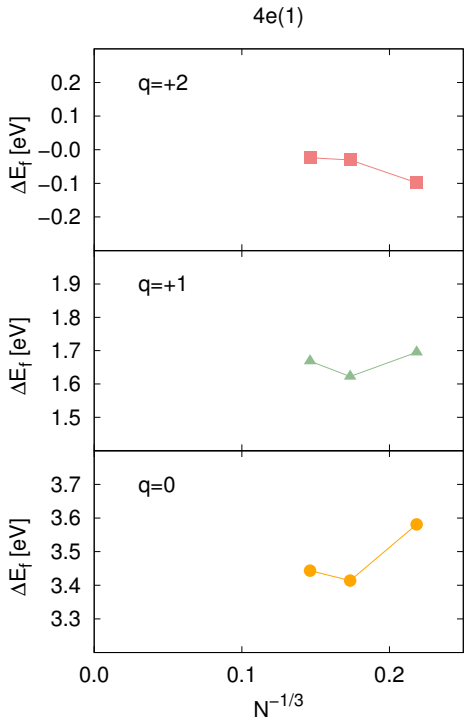

Figure 6.28: Finite size scaling for an oxygen vacancy in WO_3 in space group $P2_1/c$ located at Wyckoff site 4e(1). The chemical potential of oxygen is $1/2E_T[O_2]$ and the relative chemical potential of electrons ($\Delta\mu_e$) is 0 eV.

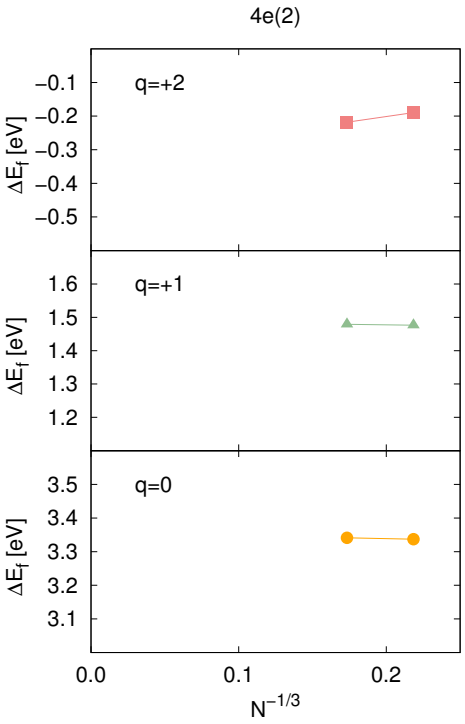

Figure 6.29: Finite size scaling for an oxygen vacancy in WO_3 in space group Pc located at Wyckoff site 4e(2). The chemical potential of oxygen is $1/2E[O_2]$ and the relative chemical potential of electrons ($\Delta\mu_e$) is 0 eV.

There has been some other studies on neutral oxygen vacancy formation energy in monoclinic WO_3 where the reported formation energies are: 4.53, 4.41, 3.46 eV [49] for the different oxygen sites. This has been calculated with a supercell consisting of 32 atoms which would explain why the large values from that study is

lower in this work. The difference may also arise because different functionals has been used, in this work vdW-DF-CX is used and in the other work by [49] the revised PBE is used. Another study [50] conducted with PBE finds the formation energies for monoclinic WO_3 to be 3.52, 3.06, 2.87 eV for the different sites in a 72 atom supercell.

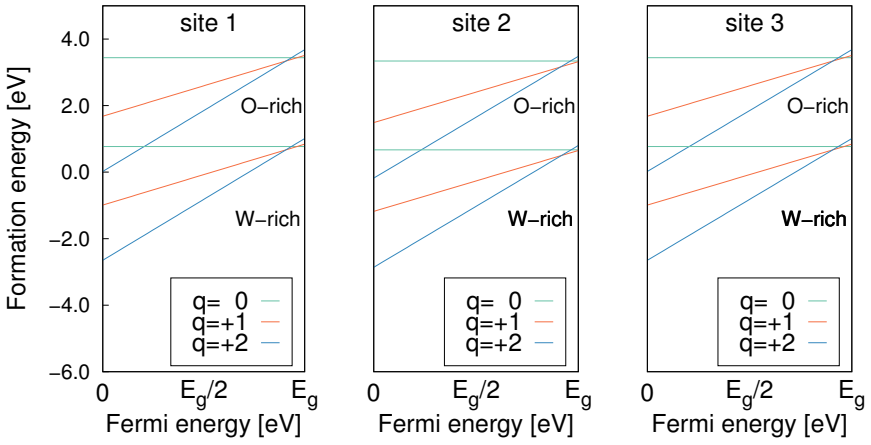

Figure 6.30: Formation energy of oxygen vacancy in WO_3 in space group $P2_1/c$ for O-rich environment and W-rich environment (see Figure 3.5). The relative electron chemical potential is allowed to vary between the valence band maximum and the conduction band minimum.

6.4.2 W vacancy

The tungsten vacancy in WO_3 is associated with a very high formation energy with respect to tungsten. The result for the most stable charge states ($-6, -5$ and -4) is compiled in Table 6.8 and the finite scaling is shown in Figure 6.31. The tungsten vacancies can have high charge states, which requires large supercells to obtain converged values for the formation energies. In contrast to oxygen vacancies for which most of the finite size effect had vanished at a 96 atom supercell, the finite size effect for the tungsten vacancies is starting to level off at the 320 atom supercell.

Table 6.8: Formation energy of tungsten vacancy in WO_3 in space group $P2_1/c$ in units of eV. The relative chemical potential of electrons ($\Delta\mu_e$) is 0 eV.

q	O-rich	W-rich
0	9.93	17.73
−1	9.44	17.23
−2	10.08	17.87
−3	10.20	18.99
−4	10.64	18.43
−5	11.07	18.87
−6	11.48	19.29

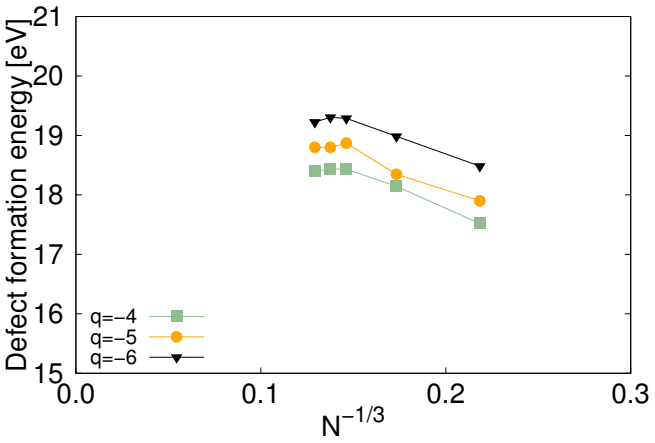

Figure 6.31: Finite size scaling of a tungsten vacancy in WO_3 in space group $P2_1/c$ for the vacancies with the highest charge states.

The neutral tungsten vacancy is not stable for any value of the relative chemical potential within the band gap, but from the VBM to 0.4 eV above the tungsten vacancy in charge state −1 is stable, there is a charge transition state between the $-1/-6$ at 0.4 eV above the VBM and from the charge transition level to the CBM the tungsten vacancy in charge state −6 is stable.

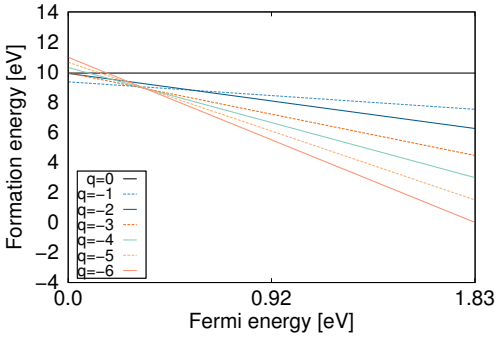

Figure 6.32: The formation energy of charged tungsten vacancies in the O-rich limit as a function of relative chemical potential.

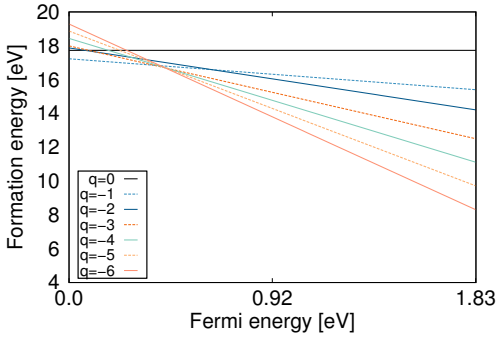

Figure 6.33: The formation energy of charged tungsten vacancies in the W-rich limit as a function of relative chemical potential.

6.4.3 Oxygen interstitials

Oxygen interstitials in WO_3 can exist in different charge states as the oxygen vacancy defect. In this work only the neutral interstitial has been considered and the formation energies are compiled in Table 6.9.

Table 6.9: Oxygen interstitial formation energy in units of eV. The supercell used in the calculations consisted of 96 atoms. The position refers to the configurations shown in Figure D.1-D.9 in Appendix D.

Position	O-rich	W-rich	Position	O-rich	W-rich
1	1.18	3.85	6	2.80	5.47
2	1.22	3.89	7	2.68	5.35
3	4.08	6.75	8	2.32	4.99
4	2.97	5.64	9	2.49	5.16
5	2.67	5.34			

The oxygen interstitials configurations in cases 1 and 2 resemble an oxygen molecule, suggesting that it is not split interstitials but rather oxygen molecule that occupies a lattice point. This defect is the most thermodynamically favorable oxygen addition. Its formation energy is quite high in the O-rich limit meaning that at low temperatures there should be a strong tendency not to form oxygen excess WO_3 phases. Configuration 1 and 4 are shown in Figure 6.34 and 6.35, respectively, where in the latter case an oxygen interstitial is placed in the unoccupied perovskite A-position. In Figure 6.34 the oxygen interstitial is paired with an oxygen in the octahedral network.

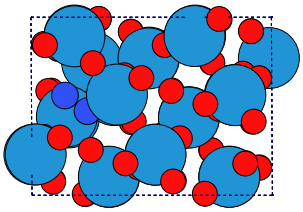

Figure 6.34: Oxygen interstitial configuration no.1. The dark blue atoms is oxygen atoms paired up with with an oxygen-oxygen distance of 1.45 Å.

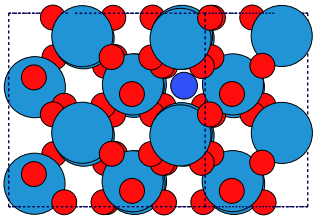

Figure 6.35: Oxygen interstitial configuration no. 4 where the oxygen interstitial is located in a void in the WO_3 structure.

6.4.4 Yttrium substitutional defects

Introducing a substitutional Y atom in WO_3 gives for a 96-atom supercell a yttrium concentration of 4.3 mole %. The yttrium atom has its nearest image 9.46 Å away, a distance for which the Y-Y interaction is small as seen in Figure 6.36. The expected charge states are VI+ for W and III+ for Y. The Y^{+3} is anticipated to be the most stable vacancy in the reference material Y_2O_3. Therefore, the substitutional reaction $W^{+6} \rightarrow Y^{+3}$ to create a -3 charged substitutional defect was the main case considered for Y substitutional defects.

In order to compute the formation energy of an yttrium substitutional defect the chemical potential of yttrium has been determined. The computed value of the formation energy (with vdW-DF-CX) of yttria is -19.18 eV to be compared to the experimental value of -20.03 eV [51]. The cohesive energy of Y in HCP is 4.166 eV, in good agreement with the experimental value of 4.37 eV [9].

Table 6.10: Y-O distances in units of Å.

	Y-O
O1	2.14
O2	2.20
O3	2.19
O4	2.14
O5	2.28
O6	2.13

The nature of the reactants makes the substitutional defect exhibit the same complexity as the charged vacancy calculations, so image charge corrections and potential alignment has been taken into account.

The formation energy of an substitutional Y defect in charge state -3 is 5.31 eV at the VBM and -0.17 eV at the CBM. The neutral substitutional Y defect has a formation energy of 4.85 eV. The chemical potential in this case corresponds to a situation in which the Y reservoir is Y_2O_3 and the oxygen reservoir is oxygen gas. The total energy difference

between the defect free and the Y-substituted system is shown in Figure 6.36. The Y substitutional defect contribute in the octahedral arrangement of WO_3 but the bond lengths differ from the ideal case, these bond lengths can be seen in Table 6.10. In comparison with pure WO_3 in Table 6.2, the bond lengths are longer on average.

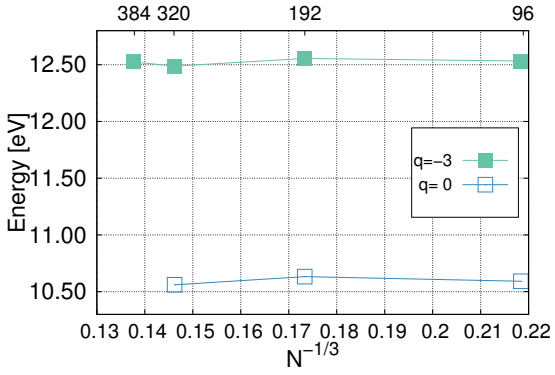

Figure 6.36: Total energy difference between ideal and defect system for Y substitutional in WO_3 in space group $P2_1/c$ for different supercell sizes.

The projected density of states resulting from insertion of an yttrium atom is shown in Figure 6.37. There is not much difference from the ideal structure in Figure 6.5 but some differences are apparent: the small bump in the Y-substitutional PDOS just below the CBM is not seen in the ideal case and the peak around 4 eV is not as pronounced in the Y-case as in the ideal.

6.4.4.1 Lattice dynamics of Y-doped WO_3.

The full phonon dispersion relation for WO_3 with substitutional Y is not easily accessible because of the associated computational cost. The derivative in equation (3.3) is evaluated by displacing the individual atoms and computing the resulting forces. Crystals with relative high symmetry such as monoclinic WO_3 in space group $P2_1/c$ require for example the evaluation of 24 distinct configurations in order to obtain the force constant matrix. Addition of a defect reduces the symmetry of the crystal. In order to compute the full force constant matrix for a configuration which exhibits $P1$-symmetry, each atom has to be displaced in each cartesian direction both forward and backward. This implies that for example already in the case of a single Y substitutional defect in a 96-atom supercell one has to compute the forces of 576 distinct configurations.

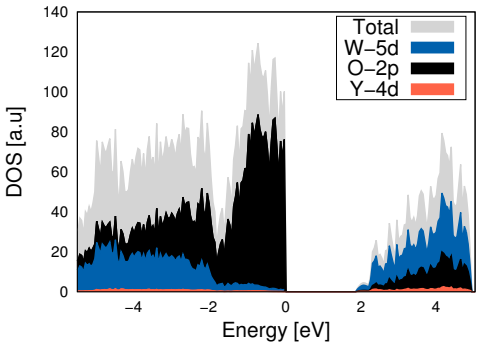

Figure 6.37: Partial density of states for monoclinic WO_3 with substitutional Y. The difference is small except for the bump close to the CBM which is not present in the defect free system.

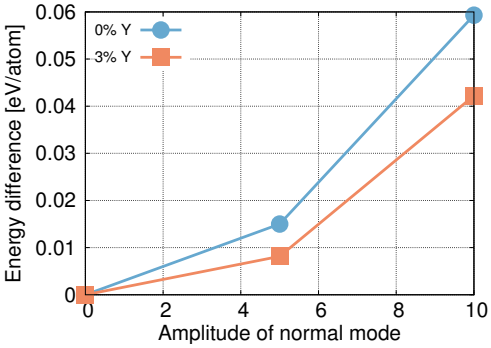

Figure 6.38: Energy difference between ideal and substitutional Y for normal mode displacements in monoclinic WO_3 in space group Pc, where the maximal amplitude of 10 corresponds to a tungsten displacement of 0.3 Å. The phonon is the first real acoustic mode at a wave vector of 0.125 in k_z-direction. The size of the supercell was $1 \times 1 \times 8$.

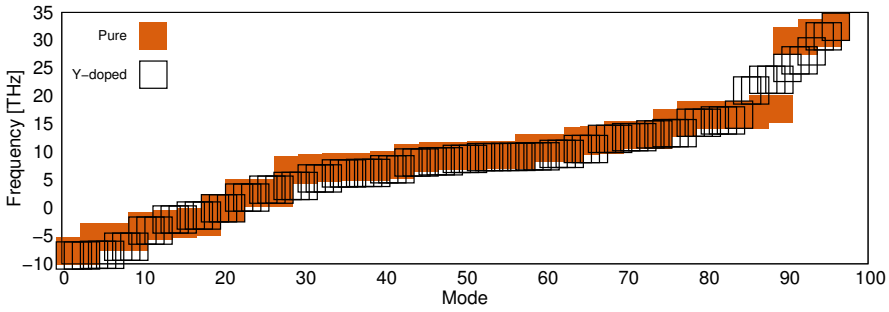

Figure 6.39: Frequency of modes for Y substitioned cubic WO_3 compared with ideal system. The Y content is 12.5 mole %.

Even with modern computers this is a formidable computation to perform. Therefore, in the present work another approach based on eigenmode following was taken. For a number of low-frequency modes the ideal structure was displaced along the normal mode and the potential energy was recorded as a function of amplitude. Utilizing the displacement pattern of the ideal system an Y substitutional defect was introduced in the displaced configurations and the the potential energy as a function of amplitude was obtained. In Figure 6.38 a representative case for the lowest frequency phonon at $q = (0, 0, 1/8)$ is shown. The introduction of Y

actually causes a further softening of the mode. This further suggests that the stability of WO_3 is not directly enhanced by yttrium since the potential landscape is related to the stiffness of the spring constant associated with vibrational motion.

The particular displacement pattern that is used to map out the potential landscape might change if Y is added to the system, therefore, the phonon dispersion has been calculated for simpler systems with higher symmetry.

The Γ-point frequencies were calculated for the ideal cubic phase with charge neutral substitutional Y to study the effects of differences in mass and electronic structure on the vibrations. A 32 atom cell with one Y atom has been used, corresponding to 12.5 mole %. This gives rise to the emergence of additional imaginary modes at Γ, the structure becomes more unstable with dopant than without further suggesting that the Y alone rather causes the structure to become more unstable. This can be seen in Figure 6.39 where the lowest frequency modes for pure and doped material are shown.

7 Discussion

7.1 Structure

There is a significant difference in how the different exchange correlation functionals describe the different oxide structures. In WO_2 the lattice parameters (Figure 5.2 and 5.3) are described in a similar manner with all functionals yielding at least decent agreement with experimental data. In WO_3, all functionals considered (PBE, PBEsol, AM05 and vdW-DF-CX, HSE06) gives a satisfactory description of the lattice geometry for the monoclinic structures (Pc and $P2_1/c$), however, the vdW-DF-CX gives the best description with respect to experimental structural parameters. The different phases of WO_3 are all associated with similar formation energies where the total energy differences between the structures are on the order of meV, but vdW-DF-CX and PBEsol accurately predicts the monoclinic structures as the structures with the lowest energy. Also, the vdW-DF-CX provides the most accurate description of the octahedral tilting, which is not captured by the other functionals except for HSE06.

In layered materials vdW interactions are known to be important and the most famous case is perhaps graphite, where the layers are bonded by vdW interactions at a distance of 3.3 Å and has successfully been described with vdW type functionals [52]. WO_3 can be seen as a layered material with alternating WO_2 and O planes separated by a distance of around 2 Å, the oxygen bond length in the z-direction.

The small energy differences between the different crystal structures of WO_3 are not unique for this type of material. $BaTiO_3$ which also is a ferroelectric material with different crystal structures such as cubic, tetragonal, and rhombohedral. There has been theoretical studies on the different structures of this material and the energy difference is in many cases on the same order, around 5 meV [53]. In WO_3, this small energy difference between the different structures is manifested in the coexistence of triclinic and monoclinic structures that is seen experimentally.

In the orthorhombic and tetragonal structures there are two experimentally proposed oxygen configurations. In the orthorhombic structure $Pcnb$ [15], the oxygen octahedral is tilted and in $Pnma$ [16]it is not. Similarly in the tetragonal case: $P4/ncc$[15] is tilted while $P4/nmm$ [18] is not. $P\bar{4}2_1m$[17] has a lower degree of tilting than $P4/ncc$. The energy difference calculated with vdW-DF-CX for the orthorhombic case is 30 meV per formula unit and 13 meV in the tetragonal case (between $P4/ncc$ and $P4/nmm$) suggesting that the tilted structures generally are

more stable than the non-tilted structures. The difference between these configurations is most prominent in the band structure. In the band structure it is mainly the valence band that is affected since it consists of oxygen states. This can be seen in Figures 6.9 and 6.10 for the orthorhombic phases and in Figures 6.11,6.12 and 6.13 for the tetragonal phases.

7.2 Phonons

WO_3 is a a very soft material and from the first principle phonon calculations all phases are unstable as no phase possesses a completely real phonon dispersion relation. While many of the phases has multiple imaginary zone center phonons, which signals an unstable unit cell the monoclinic phases (Pc and $P2_1/c$) have only one imaginary acoustic mode close to the zone center. WO_2 on the other hand does not experience the same type of instabilities since both phases of WO_2 have real phonon dispersion relations.

Studies on phonon dispersion of polar insulators has been performed earlier, for example SbS_3 [54] which also experiences long ranged interaction between atoms in the material. To properly describe the phonon dispersion, the supercell had to be relatively large (around 300+ atoms) which is significantly larger than the supercells used for phonon calculations in the present work. The reason that such large unit cells had to be used was to reduce the effect of periodic images on the elements of dynamical matrix that is not exact.

WO_3 is obviously a different material, but there are some similarities with SbS_3 such as relatively large maximum values of the Born effective charges, the maximum value is 7 in SbS_3 [54] and 10 in WO_3. The large value of the Born effective charge is also a characteristic for ferroelectric perovskites [55], in $BaTiO_3$ the maximum Born effective charge is around 7 and a similar situation is seen in $SrTiO_3$.

Since the imaginary mode was not resolved, the possibility that it is a real instability was considered and attempts to obtain a lower energy structure by mode following did not succeed. The fact that the the imaginary mode in WO_3 in space group $P2_1/c$ is not captured by larger supercells and mode following (Figure 6.22) suggests that the instability is rooted in the effect of periodic images on the dynamical matrix.

The imaginary phonon in WO_3 in space group $P2_1/c$ involves the in-plane motion of oxygen atoms in the O-plane. The undistorted crystal of WO_3 has a high degree of charge localization around the oxygen atoms in the O-plane. This means that there is little interaction between the layers, and a small displacement of the oxygen in the O-plane is associated with energy shifts of 0.4 meV/atom (Figure 6.23). For the first fully real acoustic mode the energy shift is around

50 meV/atom for the same amplitude of the mode. This also provides a hint as to why Y alone has no stabilizing effect since the bond lengths are similar and localization of charge on the oxygens may still be there.

In the present context it is of interest to consider the phonon dispersion in Na_xWO_3 [56], that is,n-doped WO_3 stabilized in the cubic structure at temperatures above 150 K. This cubic material is metallic and experiences so called Kohn anomalies in the dispersion which essentially means that there is a sharp change in the phonon dispersion such that the group velocity is discontinuous. WO_3 is a semiconducting material so should not experience Kohn anomalies but the behavior of the acoustic mode is reminiscent of a Kohn anomaly. There are studies suggesting that Kohn anomaly may be possible in Peierls semiconductors [57], however, these are usually associated with finite q and not limiting wave vectors as $q \to 0$.

7.3 Defects

7.3.1 Oxygen vacancy

There are three distinct oxygen sites in WO_3 in space group $P2_1/c$, which all have very similar vacancy formation energies as is shown in Figure 6.30. The neutral vacancy formation energy is around 3.45 eV in the O-rich limit. The distinct oxygen sites are relatively alike, especially the Wyckoff sites 4e(1) and 4e(3) which are both located in the WO_2-plane with similar bond lengths to the central tungsten atom. The oxygen atom on Wyckoff site 4e(2) resides in the O-plane with slightly different bond lengths to the center tungsten atom, however, this small difference in bond length does not have a major effect on the vacancy formation energy. The neutral oxygen vacancy formation for a vacancy located on the Wyckoff site 4e(2) is 0.1 eV lower than for the other two sites. Furthermore, the oxygen vacancy located on Wyckoff site 4e(2) is associated with only one charge transition level (+2/+1) at 0.15 eV below the CBM while there are two charge transition levels in the other two cases. In comparison with WO_2, which does not exhibit charged vacancies, the smallest value of the neutral oxygen vacancy formation energy has a value of 0.77 eV in WO_3 and a value of 2.48 eV in WO_2. In WO_2 as opposed to WO_3 the energy difference between the two distinct oxygen positions is quite high, at a value of 0.5 eV.

The neutral oxygen vacancy in WO_3 introduces a relaxation of the tungsten atoms away from the defect center by as much as 0.3 Å, which is slightly above 10% of the tungsten oxygen bond length. The relaxation between different charge states are significantly smaller, only 0.04 Å between the neutral and +1 charged state. Large structural differences between different charge states indicate the

presence of deep traps. In metallic systems the notion of traps is not important since there is no band gap, however, for comparison, the WO_2 relaxation around a neutral defect is 0.15 Å. This relaxation distance is considerably shorter than the equivalent in WO_3 and could be a manifestation of the more rigid structure in WO_2.

The number of oxygen sites per volume is approximately the same in both WO_3 and WO_2, which means that differences in vacancy concentration are mainly due to the formation energies. The transport of oxygen in the oxides by vacancy migration is largely dependent on the vacancy concentration. In the O-rich limit the formation energy of the oxygen vacancy in Wyckoff site 4e(1) in WO_2 has a formation energy which is about 0.5 eV lower than the smallest oxygen vacancy formation energy in WO_3. In a W-rich environment, the formation energies decrease because of the driving force for creating oxygen deficient phases will be larger.

The formation energies of charged vacancies depend on the band gap, which is poorly described within local + semilocal density functional theory. The result in Figure 6.30 indicates that the oxygen vacancy defect creates a shallow donor in the band gap but the fact that the band gap is not properly described within DFT, may relocate the defect level if a better description was available. Studies of the ideal system with HSE06 reveal that the vdW-DF-CX equilibrium structure is not close to equilibrium with HSE06, this makes it difficult to align the band gap calculated with HSE06 to the energy calculations performed with vdW-DF-CX.

There have been some studies on monoclinic WO_3 with hybrid functionals such as [58], which predicts a band gap of 3.45 eV, and a deep defect level.

The neutral vacancy formation energy for oxygen in the high temperature tetragonal phase is not anticipated to differ much from the neutral vacancy formation energy in WO_3 in space group $P2_1/c$ because of the structural similarities between the phases. This is further suggested by a naive formation energy calculation in the tetragonal phase, which gives a difference of around 5% in the formation energy compared with the monoclinic phase. The charged defects on the other hand, may deviate substantially because of the smaller band gap.

7.3.2 Oxygen interstitial

In W the oxygen interstitial formation energy is relatively high with a value of 3.49 eV with respect to WO_2, which makes the oxygen interstitial concentration low at moderate temperatures. Two oxygen interstitials tend to pair up and bond to a tungsten atom, which is likely to be important in the formation of tungsten oxides. In both WO_2 and WO_3, the pairing of oxygen connected to a lattice point leads to the oxygen interstitial with the lowest formation energy with around 1 eV for O-rich environments. The appearance of the oxygen pair is different. In WO_2

it is a distinct split interstitial with the lattice point centered between the oxygen atoms such that the oxygens are at a distance of 2.15 Å from each other. In WO_3, on the other hand, the oxygen associated with the lattice point is not significantly moved as it is in the WO_2 configuration, and the interstitial oxygen bonds to the lattice point oxygen. Split interstitials migration may be a low energy migration path, specially in WO_2 because of the edge sharing configuration which makes the migration distance relatively short. The formation energies of split interstitials along the edge that is shared in WO_2 are however not energetically favorable as compared to other split interstitial configurations. Studies of charged interstitials in WO_3 have not been performed but are also likely to be important because of the relatively low formation energy of neutral interstitials in the O-rich limit.

7.3.3 Tungsten vacancies

The W vacancy is associated with low vacancy formation energies in W and WO_2 in the W-rich limit with formation energies of 3.70 eV in W and 2.46 eV in WO_2 in the W-rich limit. The formation energy for neutral W vacancy in WO_3 is 17.73 eV. In the case of WO_3 different charge states are stable and this behavior over the band gap makes some W vacancies in WO_3 likely to be important, specifically the vacancies with charge states -1 and -6. The large states involved imply huge corrections since the Makov-Payne correction scales as q^2. Therefore, the charge transition levels depend sensitively on the formation energy, but also the formation energy is prone to errors because of the large charge states.

For the -6 charge state an error in the correction term of 10 meV means that the vacancy formation energy has an error of 0.36 eV, which makes the dilute limit concentration differ by a factor of 65 at 1000 K.

7.3.4 Yttrium substitutional defect

The Y substitutional defect is associated with a formation energy of 5.31 eV at the VBM to -0.18 eV at the CBM, the negative formation energy plainly means that WO_3 is unstable with respect to formation of substitutional Y defect for such large electro-chemical potentials. The impact of substitutional Y defects on the lattice of dynamics was studied by mapping the potential energy landscape associated with the normal modes of the defect free system. By displacing the crystal structure along the imaginary normal mode of the defect free system, the potential energy is in all cases more negative with Y-doping than without. This means that Y is actually making the system more soft. In the present work only the effect of a single substitutional Y has been considered, but this is a simplified picture. The normal modes of the Y-doped material could change, making the studied normal mode invalid in the presence of Y-doping. There is yet another

simplification present, namely that the substitutional Y-defect would cause the formation of other defects in the system by charge neutrality conditions, which has not been considered in this study. In that case, oxygen vacancy defects could be formed which could in turn influence the lattice dynamics.

Studies has been performed on YSZ [59], where the charge neutrality condition is imposed by creation of +2 charged oxygen vacancies at 4.11 Å from the Y atoms. Zirconia is different material than WO_2 and WO_3 but the mechanism of stabilization might be similar. If the mechanism is to form composite defects then the dilute limit approximation is not feasible model to assess the thermodynamical stability between oxides and further studies are needed to understand the concentration of defects. At this point, no results support the idea that Y would stabilize WO_3, however, the Y substitutional defect may change the thermodynamic phase stability between WO_2 and WO_3 and hence stabilize the oxide in an indirect way while at the same time creating a passivating layer.

7.3.5 Accuracy of defect calculations

There are some errors associated with calculation the formation energy of point defects. Volume relaxation has been omitted because it is anticipated that the vacancy will induce a relaxation of nearby atoms only. The energy difference for a neutral oxygen vacancy in WO_3 between a system that was allowed to change volume and one that had a constant volume was found to be below 0.1 eV.

The long range force constants in WO_3 (Figure 6.24) might also influence the defect formation energies at small supercells. However, at sufficiently large supercells both these errors should be very small.

The errors that are more difficult to handle are the ones associated with ionic movement in WO_3, such as the ionic part of the dielectric tensor, which is the main contribution to the static dielectric tensor. The ionic part of the dielectric tensor is prone to the same errors as the phonon dispersion relation, since both involve phonon properties. Literature values for the static dielectric constant for WO_3 are not readily available, however measurements of the dielectric constant at 1 kHz at room temperature on thin films gives extrapolated bulk values of around 30 [60] which is similar to the static values obtained in this work, which varies between 70 and 10 approximately for the diagonal elements, however, the calculated dielectric tensors and experimental with elements of 30 give approximately the same monopole monopole correction.

8 Conclusions

Tungsten trioxide is structurally a very complex material, which makes it difficult to describe theoretically. This is manifested in the failure of several exchange correlation functionals to properly describe the atomic structure as well as the shortcomings of the hybrid functional for WO_3 in space groups Pc and $P2_1/c$ and WO_2 in space group $Pnma$. The vdW-DF-CX functional, however, accurately predicts the ground state structure and formation energies.

The phonon dispersion relation for WO_3 in space group $P2_1/c$, which is structurally very similar to the ground state structure in space group Pc, shows imaginary frequencies. The imaginary frequencies might be a result of very long range interactions in the material together with the necessarily finite system used in the simulations. In order to fully converge the phonon dispersion relation a much larger supercell should be employed, where the interactions between atoms from different supercells have vanished.

The neutral oxygen vacancy formation energy in O-rich environments is larger in WO_3 than in WO_2 when employing the proper thermodynamic boundary conditions. In WO_3, the $+2$ oxygen vacancy is stable from the valence band until around 0.15 eV below the conduction band, suggesting that it acts as a relatively shallow donor.

The band gap is still poorly described with vdW-DF-CX, which means that for proper defect calculations another approach has to be considered to be able to align the band gap. As the hybrid functional predict large forces for the vdW-DF-CX equilibrium structure, more complex many body theories are needed to correct for the band gap problem.

The introduction of Y as a substitutional defect influences the oxygen atoms closest to it, but no stabilizing effect was found. In fact, the present studies suggests that substitutional Y has the opposite effect. Although, the approach is approximate, the data obtained in this study can be used as a starting point for further studies involving charge neutrality conditions to further elucidate the role of substitutional Y on the stability of WO_3.

Bibliography

[1] H. Maier et al. Tungsten and beryllium armour development for the JET ITER-like wall project. *Nuclear Fusion*, 47(3):222, 2007.

[2] R A Pitts et al. Status and physics basis of the ITER divertor. *Physica Scripta*, 2009(T138):014001, 2009.

[3] C. Thomser et al. Plasma facing materials for the JET ITER-like wall. *Fusion science and technology*, pages 1–8, 2012.

[4] S. Kobayashi, N. Hosoda, and R. Takashima. Tungsten alloys as radiation protection materials. *Nuclear Instruments and Methods in Physics Research Section A: Accelerators, Spectrometers, Detectors and Associated Equipment*, 390(3):426 – 430, 1997.

[5] J. Kim et al. Nano-W Dispersed Gamma Radiation Shielding Materials. *Advanced Engineering Materials*, 16(9):1083–1089, 2014.

[6] M Penza et al. Tungsten trioxide (WO_3) sputtered thin films for a NO_x gas sensor. *Sensors and Actuators B: Chemical*, 50(1):9–18, 1998.

[7] G. Sberveglieri et al. WO_3 sputtered thin films for NO_x monitoring. *Sensors and Actuators B: Chemical*, 26(1–3):89–92, 1995.

[8] A Paliwal et al. Room temperature detection of NO_2 gas using optical sensor based on surface plasmon resonance technique. *Sensors and Actuators B: Chemical*, 216:497–503, 2015.

[9] C. Kittel. *Introduction to solid state physics*. John Wiley & Sons, 8th edition, 2005.

[10] T. Hahn, editor. *International Table for Crystallography volume A: Space-Group Symmetry*. Springer, 5 edition, 2005.

[11] E Salje et al. Crystal structure and paramagnetic behaviour of ε-WO_3. *Journal of Physics: Condensed Matter*, 9(31):6563, 1997.

[12] R. Diehl, G. Brandt, and E. Salje. The crystal structure of triclinic WO_3. *Acta Crystallographica Section B*, 34(4):1105–1111, 1978.

[13] B.O Loopstra and P Boldrini. Neutron diffraction investigation of WO_3. *Acta Crystallographica*, 21:158–162, 1966.

[14] Y Xu et al. Single-crystal diffraction studies of WO_3 at high-pressures and structure of a high pressure WO_3 phase. *Journal of solid state chemistry*, pages 123–130, 1997.

[15] T. Vogt, P.M. Woodward, and B.A. Hunter. The High-Temperature Phases of WO_3. *Journal of Solid State Chemistry*, 144:209–215, 1999.

[16] E. Salje. The Orthorhombic Phase of WO_3. *Acta Cryst.*, B33:574–577, 1976.

[17] I.J. McColm, R. Steadman, and S.J Wilson. Iron-promoted phases in the tungsten oxygen system. *Journal of Solid State Chemistry*, 23:33–42, 1977.

[18] W.L. Kehl, R.G. Hay, and D. Wahl. The Structure of Tetragonal Tungsten Trioxide. *Journal of Applied Physics*, 23(2), 1952.

[19] B. Gerand et al. Structural Study of a New Hexagonal Form of Tungsten Trioxide. *Journal of Solid State Chemistry*, 29:429–434, 1979.

[20] J. Oi, A. Kishimoto, and T. Kudo. Hexagonal Tungsten Trioxide Obtained from Peroxo-polytungstate and Reversible Lithium Electro-intercalation into its Framework. *Journal of Solid State Chemistry*, 96:13–19, 1992.

[21] G. Vineyard. Frequency factors and isotope effects in solid state rate processes. *Journal of Physics and Chemistry of Solids*, 3:121–127, 1957.

[22] P. Hohenberg and W. Kohn. Inhomogeneous Electron Gas. *Phys. Rev.*, 136:B864–B871, 1964.

[23] W. Kohn and L. J. Sham. Self-Consistent Equations Including Exchange and Correlation Effects. *Phys. Rev.*, 140:A1133–A1138, 1965.

[24] R.M. Martin. *Electronic structure: Basic Theory and Practical Methods*. Cambridge university press, 3^{th} edition, 2004.

[25] J.M Thijssen. *Computational Physics*. Cambridge University Press, 2nd edition, 2007.

[26] J.P. Perdew, K. Burke, and M. Ernzerhof. Generalized gradient approximation made simple. *Phys. Rev. Lett.*, 77:3865–3868, 1996.

[27] J. Perdew et al. Restoring the density-gradient expansion for exchange in solids and surfaces. *Phys. Rev. Lett.*, 100:136406, 2008.

[28] R. Armiento and A. E. Mattsson. Functional designed to include surface effects in self-consistent density functional theory. *Phys. Rev. B*, 72:085108, 2005.

[29] K. Berland and P. Hyldgaard. Exchange functional that tests the robustness of the plasmon description of the van der Waals density functional. *Phys. Rev. B*, 89:035412, 2014.

[30] J. Heyd, G.E. Scuseria, and M. Ernzerhof. Hybrid functionals based on a screened Coulomb potential. *Journal of Chemical Physics*, 118(18), 2003.

[31] G. Kresse and J. Hafner. *Ab initio* molecular dynamics for liquid metals. *Phys. Rev. B*, 47:558–561, Jan 1993.

[32] G. Kresse and J. Furthmüller. Efficiency of ab-initio total energy calculations for metals and semiconductors using a plane-wave basis set. *Computational Materials Science*, 6(1):15 – 50, 1996.

[33] G. Kresse and J. Furthmüller. Efficient iterative schemes for *ab initio* total-energy calculations using a plane-wave basis set. *Phys. Rev. B*, 54:11169–11186, Oct 1996.

[34] G. Kresse and D. Joubert. From ultrasoft pseudopotentials to the projector augmented-wave method. *Phys. Rev. B*, 59:1758–1775, Jan 1999.

[35] A Togo and I Tanaka. First principles phonon calculations in materials science. *Scr. Mater.*, 108:1–5, 2015.

[36] G. Makov and M. C. Payne. Periodic boundary conditions in *ab initio* calculations. *Phys. Rev. B*, 51:4014–4022, 1995.

[37] S. Lany and A. Zunger. Assessment of correction methods for the band-gap problem and for finite-size effects in supercell defect calculations: Case studies for ZnO and GaAs. *Phys. Rev. B*, 78:235104, 2008.

[38] J.D. Gale and A.L. Rohl. The general utility lattice program (GULP). *Molecular Simulation*, 29(5):291–341, 2003.

[39] P Erhart et al. First-principles study of codoping in lanthanum bromide. *Phys. Rev. B*, 91:165206, 2015.

[40] S. Giusepponi and M. Celino. The effects of vacancies in the mechanical properties of tungsten: A first-principles study. *Nuclear Instruments and Methods in Physics Research Section B: Beam Interactions with Materials and Atoms*, 342:70 – 75, 2015.

[41] A Alkhamees et al. First-principles investigation on dissolution and diffusion of oxygen in tungsten. *Journal of Nuclear Materials*, 393(3):508 – 512, 2009.

[42] J.N Mundy, S.T S.T. Ockers, and L.C Smedskjaer. Vacancy Migration Enthalpy in Tungsten at High Temperatures. *Materials Science Forum*, 15-18:199–204, 1987.

[43] A. A. Bolzan, B. J. Kennedy, and C. J. Howard. Neutron powder diffraction study of molybdenum and tungsten dioxides. *Australian Journal of Chemistry*, 48:1473–1477, 1995.

[44] M. Sundberg, P. Werner, and I. Zibrov. X-ray powder crystal structure analysis of high pressure tungsten dioxide. On the information in weak reflections. *Zeitschrift für Kristallographie-Crystalline Materials*, 209(8):662–666, 2010.

[45] A.D. Mah. The heats of formation of tungsten trioxide and tungsten dioxide. *Journal of the American Chemical Society*, 81(7):1582–1583, 1959.

[46] P. P. González-Borrero et al. Optical band-gap determination of nanostructured WO_3 film. *Applied Physics Letters*, 96(6), 2010.

[47] P.M. Vogt, T. Woodward and A.W. Sleight. Ferroelectric Tungsten Trioxide. *Journal of Solid State Chemistry*, 131, 1997.

[48] K.R Locherer, Swainson. I.P, and E Salje. Phase transitions in tungsten trioxide at high temperatures - a new look. *Journal of Physics: Condensed Matter*, 11(35):6737, 1999.

[49] R. Chatten et al. The Oxygen Vacancy in Crystal Phases of WO_3. *The Journal of Physical Chemistry B*, 109(8):3146–3156, 2005.

[50] C Lambert-Mauriat et al. Ab initio study of oxygen point defects on tungsten trioxide surface. *Surface Science*, 606(1–2):40 – 45, 2012.

[51] L.R Morss et al. Standard molar enthalpies of formation of Y_2O_3, Ho_2O_3 and Er_2O_3 at the temperature 298.15 K. *The Journal of Chemical Thermodynamics*, 25:415–422, 1993.

[52] M. Birowska, K. Milowska, and J.A Majewski. Van Der Waals Density Functionals for Graphene Layers and Graphite. *Acta Physica Polonica A*, 120, 2011.

[53] H Moriwake, C.A.J Fisher, and A Kuwabara. First-principles Calculations of the Phase Transition in $CaTiO_3$ under Negative Static Pressure. *Journal of the Korean Physical Society*, 59:2497–2502, 2011.

[54] Yun Liu et al. First-principles study of the lattice dynamics of Sb_2S_3. *Phys. Chem. Chem. Phys.*, 16:345–350, 2014.

[55] W. Zhong, R. D. King-Smith, and D. Vanderbilt. Giant LO-TO splittings in perovskite ferroelectrics. *Phys. Rev. Lett.*, 72:3618–3621, 1994.

[56] W. A. Kamitakahara et al. Concentration-Dependent Kohn Effect in Cubic Tungsten Bronzes. *Phys. Rev. Lett.*, 36:1393–1396, 1976.

[57] H. Rietschel. The giant Kohn phonon anomaly in a Peierls semiconductor. *Solid State Communications*, 13(11):1859 – 1863, 1973.

[58] M Gerosa et al. Defect calculations in semiconductors through a dielectric-dependent hybrid DFT functional: The case of oxygen vacancies in metal oxides. *The Journal of Chemical Physics*, 143(13), 2015.

[59] A. Eichler. Tetragonal Y-doped zirconia: Structure and ion conductivity. *Phys. Rev. B*, 64:174103, 2001.

[60] S.K Deb. Optical and photoelectric properties and colour centres in thin films of tungsten oxide. *Philosophical magazine*, 27, 1973.

A Structural parameters

In this section the different exchange correlation functionals and error compared with experiment is reported. The number above the figures refer to the International Table of Crystallography [10].

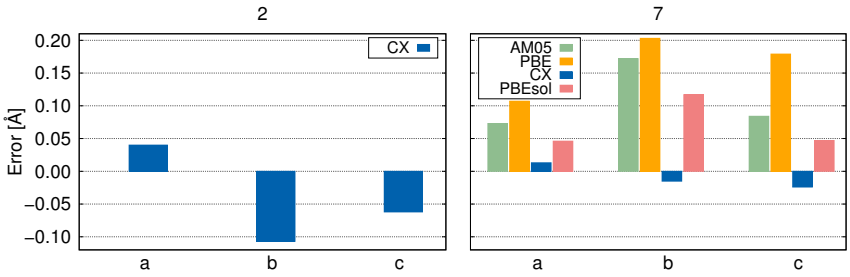

Figure A.1: Error between computed and experimental lattice parameters for $P\bar{1}$ (ITC no. 2) and Pc (ITC no. 7).

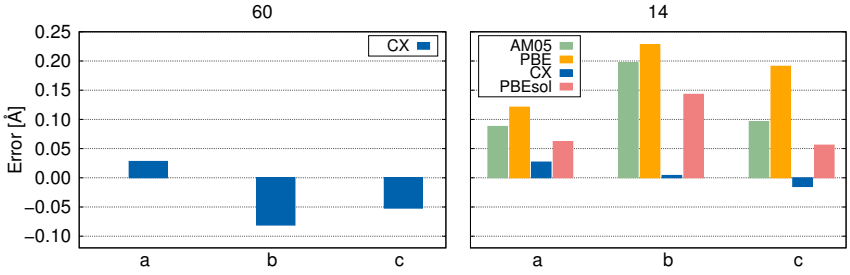

Figure A.2: Error between computed and experimental lattice parameters for $P2_1/c$ (ITC no. 14) and orthorhombic WO_3 in space group $Pcnb$ (ITC no. 60).

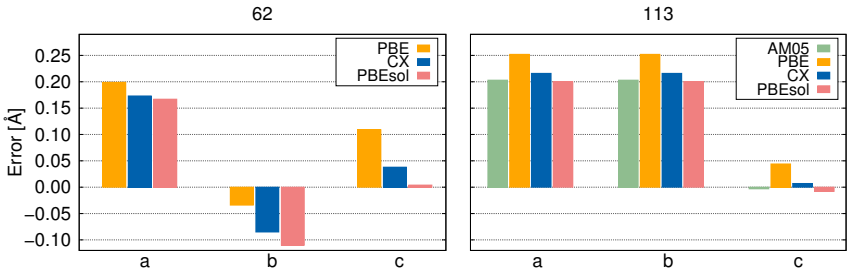

Figure A.3: Error between computed and experimental lattice parameters for orthorhombic WO_3 in space group $Pnma$ (ITC no. 62) and tetragonal WO_3 in space group $P\bar{4}2_1m$ (ITC no. 113).

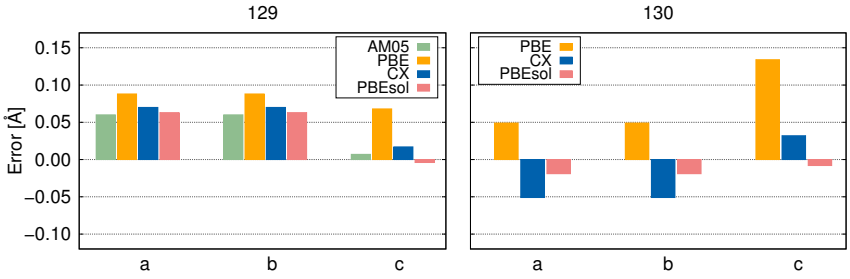

Figure A.4: Error between computed and experimental lattice parameters for tetragonal WO_3 in space group $P4/nmm$ (ITC no. 129) and tetragonal WO_3 in space group $P4/ncc$ (ITC no. 130).

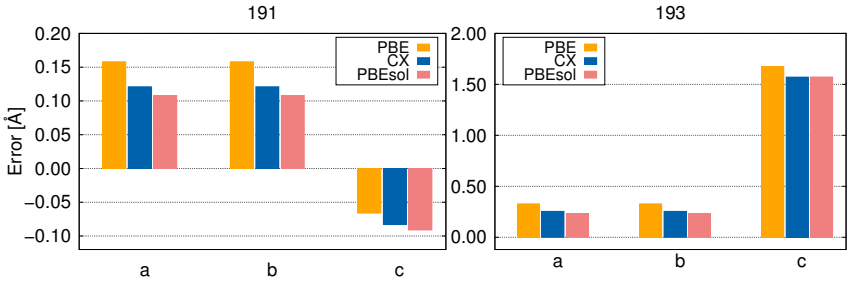

Figure A.5: Error between computed and experimental lattice parameters for hexagonal WO_3 in space group $P6/mmm$ (ITC no. 191) and hexagonal WO_3 in space group $P6_3/mcm$ (ITC no. 193).

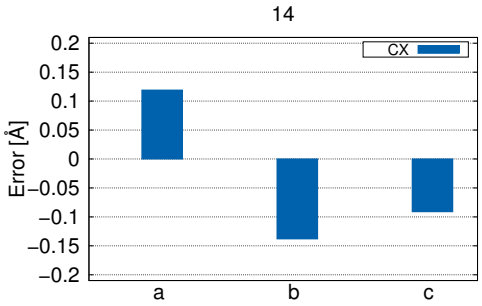

Figure A.6: Error between computed and experimental lattice parameters for monoclinic WO_3 in space group $P2_1/n$ (ITC no. 14).

B Force convergence

The phonons are sensitive to the accuracy of the force calculations, therefore, the influence of some of the critical parameters on the phonon dispersion relation has been investigated. The parameters in `VASP` and `phonopy` that has been investigated are: electronic convergence critereon: *EDIFF*, the fast fourier mesh: *ADDGRID*, the real space and reciprocal space projection: *LREAL*, the displacement length in `phonopy` and the minimum number of self consistent cycles: *NELMIN*. The system under consideration is the unstable ideal cubic structure because of its high symmetry and small unit cell and therefore low computational cost.

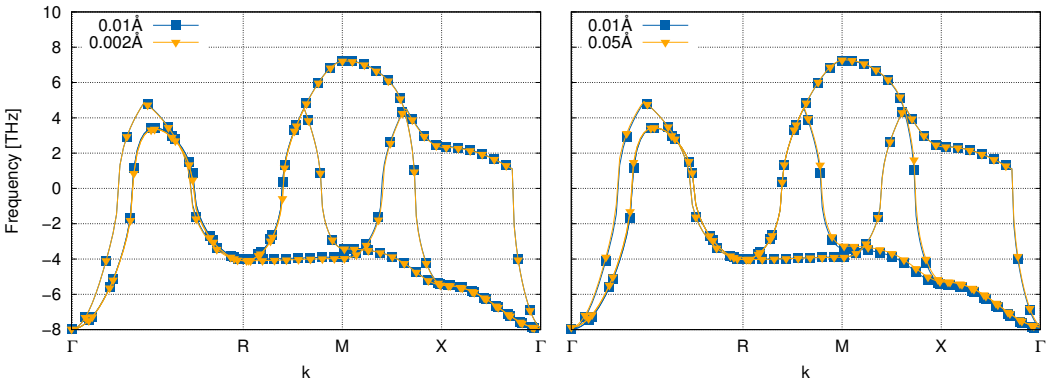

Figure B.1: The displacement length in phonopy effect on phonon dispersion relation.

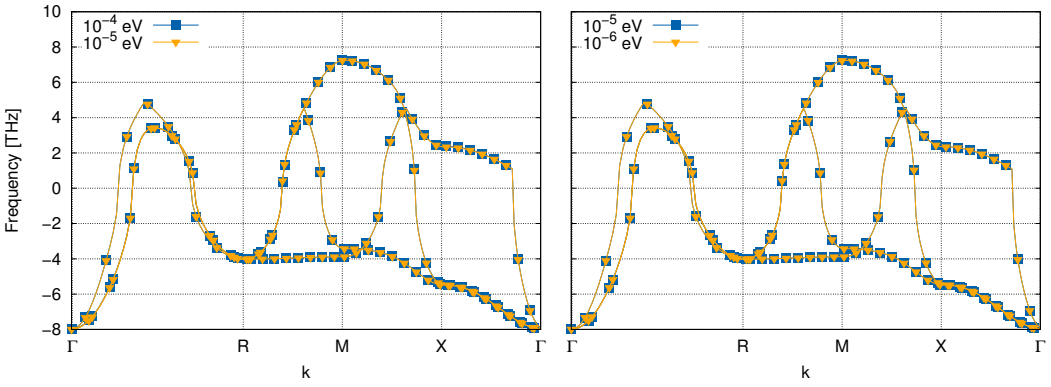

Figure B.2: The electronic density convergence critereon.

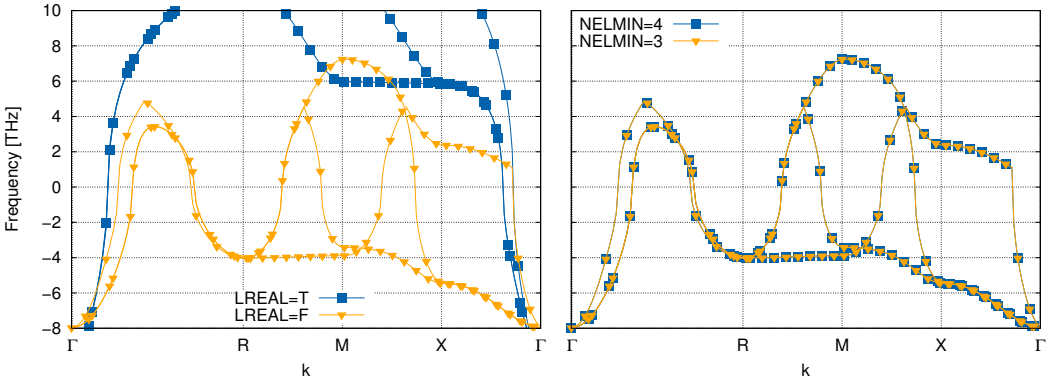

Figure B.3: The real space vs reciprocal space projector operators to the left and the minimum number of self consistent loops to the right.

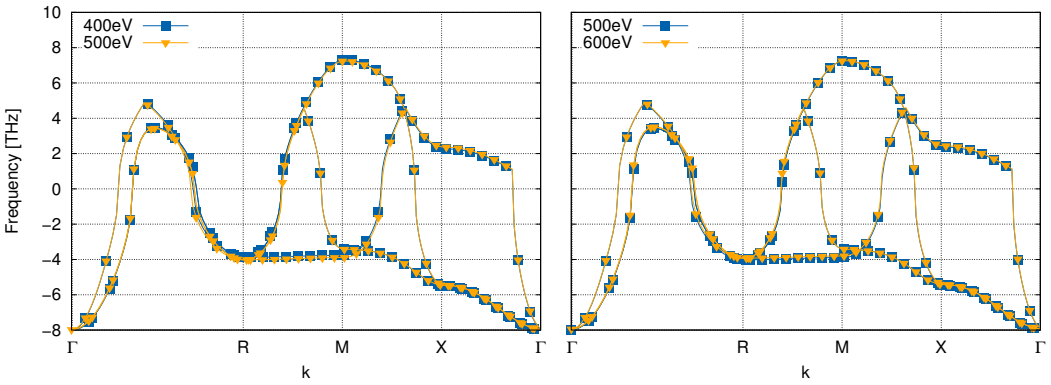

Figure B.4: Plane wave cut off energy effect on phonon dispersion.

C Dielectric function and Born effective charges

C.1 WO_3 in space group $P2_1/c$

The dielectric function for WO_3 calculated with CX and 16 atom unit cell is:

$$\varepsilon = \begin{pmatrix} 72.00 & 0.00 & -1.93 \\ 0.00 & 38.73 & 0.00 \\ -1.93 & 0.00 & 8.32 \end{pmatrix} \tag{C.1}$$

In WO_3, there are three unique oxygen positions and one unique tungsten position. For these unique positions the Born effective charges are:

$$Z^*_{O_1} = \begin{pmatrix} -4.54 & -3.076 & -0.70 \\ -2.82 & -4.01 & -0.52 \\ -4.54 & -3.08 & -0.70 \end{pmatrix} \tag{C.2}$$

$$Z^*_{O_2} = \begin{pmatrix} -4.62 & 2.88 & 0.69 \\ 2.80 & -3.87 & -0.61 \\ -4.62 & 2.88 & 0.69 \end{pmatrix} \tag{C.3}$$

$$Z^*_{O_3} = \begin{pmatrix} -1.11 & -0.01 & 0.22 \\ 0.04 & -1.23 & -0.26 \\ -1.11 & -0.01 & 0.22 \end{pmatrix} \tag{C.4}$$

$$Z^*_{W} = \begin{pmatrix} 10.28 & -1.29 & -0.21 \\ 1.14 & 9.11 & 1.40 \\ 10.28 & -1.29 & -0.21 \end{pmatrix} \tag{C.5}$$

D Oxygen interstitials in tungsten trioxide

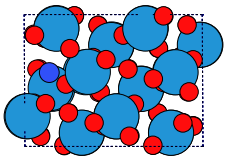

Figure D.1: Configuration 1.

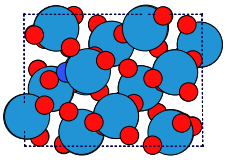

Figure D.2: Configuration 2.

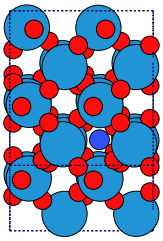

Figure D.3: Configuration 3.

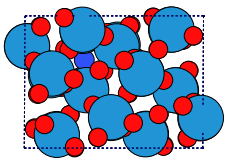

Figure D.4: Configuration 4.

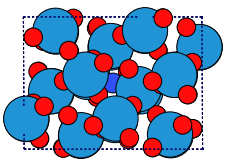

Figure D.5: Configuration 5.

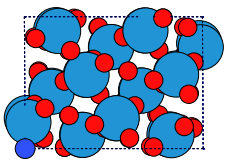

Figure D.6: Configuration 6.

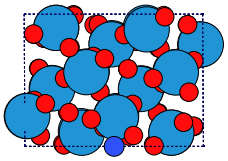

Figure D.7: Configuration 7.

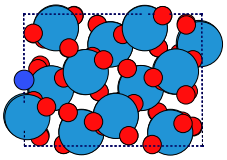

Figure D.8: Configuration 8.

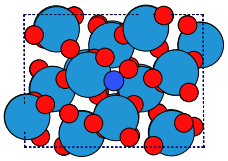

Figure D.9: Configuration 9.